Biogeosciences, 22, 555–584, 2025
https://doi.org/10.5194/bg-22-555-2025

Biogeosciences Open Access EGU

Seasonal and interannual variability in CO_2 fluxes in southern Africa seen by GOSAT

Eva-Marie Metz[1], Sanam Noreen Vardag[1,2], Sourish Basu[3,4], Martin Jung[5], and André Butz[1,2,6]

[1]Institute of Environmental Physics, Heidelberg University, 69120 Heidelberg, Germany
[2]Heidelberg Center for the Environment (HCE), Heidelberg University, 69120 Heidelberg, Germany
[3]Goddard Space Flight Center, NASA, Greenbelt, MD 20771, USA
[4]Earth System Science Interdisciplinary Center, University of Maryland, College Park, MD 20740, USA
[5]Department of Biogeochemical Integration, Max Planck Institute for Biogeochemistry, 07745 Jena, Germany
[6]Interdisciplinary Center for Scientific Computing (IWR), Heidelberg University, 69120 Heidelberg, Germany

Correspondence: Eva-Marie Metz (eva-marie.metz@iup.uni-heidelberg.de)

Received: 26 June 2024 – Discussion started: 2 September 2024
Revised: 25 November 2024 – Accepted: 26 November 2024 – Published: 30 January 2025

Abstract. The interannual variability in the global carbon sink is heavily influenced by semiarid regions. Southern hemispheric Africa has large semiarid and arid regions. However, there is only a sparse coverage of in situ CO_2 measurements in the Southern Hemisphere. This leads to uncertainties in measurement-based carbon flux estimates for these regions. Furthermore, dynamic global vegetation models (DGVMs) show large inconsistencies in semiarid regions. Satellite CO_2 measurements offer a spatially extensive and independent source of information about the southern African carbon cycle.

We examine Greenhouse Gases Observing Satellite (GOSAT) CO_2 concentration measurements from 2009 to 2018 in southern Africa. We infer CO_2 land–atmosphere fluxes which are consistent with the GOSAT measurements using the TM5-4DVar atmospheric inversion system. We find systematic differences between atmospheric inversions performed on satellite observations versus inversions that assimilate only in situ measurements. This suggests limited measurement information content in the latter. We use the GOSAT-based fluxes and solar-induced fluorescence (SIF; a proxy for photosynthesis) as atmospheric constraints to select DGVMs of the TRENDYv9 ensemble which show compatible fluxes. The selected DGVMs allow for the study of the vegetation processes driving the southern African carbon cycle. By doing so, our satellite-based process analyses pinpoint photosynthetic uptake in the southern grasslands to be the main driver of the interannual variability in the southern African carbon fluxes, agreeing with former studies based on vegetation models alone. We find that the seasonal cycle, however, is substantially influenced by enhanced soil respiration due to soil rewetting at the beginning of the rainy season. The latter result emphasizes the importance of correctly representing the response of semiarid ecosystems to soil rewetting in DGVMs.

1 Introduction

The terrestrial carbon sink currently takes up nearly one-third of anthropogenic greenhouse gases and thereby mitigates climate change (Friedlingstein et al., 2023). The amount of CO_2 taken up by global ecosystems varies substantially from year to year. This interannual variability (IAV) reflects the response of ecosystem carbon uptake to varying climate conditions, such as temperature or precipitation fluctuations (Zeng et al., 2005; Zhang et al., 2018; Piao et al., 2020). Current vegetation models struggle to accurately reproduce the IAV of the terrestrial carbon sink, and an imbalance exists between the modeled and measured total global sink estimates (Friedlingstein et al., 2023). The imbalance is even stronger when examining carbon fluxes on smaller spatial scales (Bastos et al., 2020) and implies that there is still an insufficient understanding of the terrestrial processes driving land carbon exchange. A better understanding is needed to improve climate models and climate change predictions (Steiner, 2020).

Semiarid regions contribute substantially to the IAV in the global terrestrial carbon sink. In these regions, precipitation and temperature fluctuations heavily impact the IAV in carbon fluxes (Poulter et al., 2014; Ahlström et al., 2015). Africa has large areas of semiarid and arid ecosystems (Williams et al., 2007) and contributes substantially to the global IAV (Williams et al., 2007; Valentini et al., 2014; Pan et al., 2020). However, in situ CO_2 measurements in Africa are very sparse, leading to large uncertainties in carbon flux estimates from atmospheric inversions and machine learning approaches (Valentini et al., 2014; Ernst et al., 2024). Dynamic global vegetation models (DGVMs) also show large inconsistencies amongst each other and tend to underestimate the interannual CO_2 flux variability in semiarid regions (MacBean et al., 2021).

Satellite CO_2 concentration measurements, for example, from the Greenhouse Gases Observing Satellite (GOSAT) measuring CO_2 concentrations since 2009 or the Orbiting Carbon Observatory-2 (OCO-2) launched in 2014, have much denser coverage compared with in situ measurements. Previous studies have found systematic differences between satellite-based CO_2 concentrations and fluxes in southern Africa and those based on in situ measurements (Mengistu and Mengistu Tsidu, 2020; Byrne et al., 2023). Byrne et al. (2023) attribute these differences mainly to the sparse coverage of in situ CO_2 measurements. The studies emphasize the potential of satellite-based atmospheric inversions to provide additional information and, therefore, more robust estimates of the carbon fluxes in southern Africa, which then enable research on processes driving the CO_2 exchange. Metz et al. (2023) demonstrate the potential of combining satellite-based CO_2 flux estimates with DGVMs in Australia to decipher soil respiration processes driving the Australian terrestrial CO_2 exchange at the continental scale.

Here, we investigate the decadal dataset of GOSAT CO_2 concentrations over southern Africa from 2009 to 2018. We run a global inversion with GOSAT and in situ measurements to infer GOSAT-satellite-based CO_2 exchange between the land and atmosphere and compare the results to those based on in situ measurements alone, to FLUXCOM products, and to the TRENDYv9 ensemble of DGVMs. By selecting a subset of DGVMs that match the satellite-based carbon fluxes, we analyze the underlying processes driving the IAV and seasonal variability in the southern African carbon cycle.

2 Data and methods

2.1 Study region

Our study region spans southern Africa south of 10° S including Madagascar (see Fig. 1). This region agrees with the region selection in Mengistu and Mengistu Tsidu (2020) and considers the different climatic conditions found on the African continent. North of the study region, Africa is influenced by the low-pressure system of the Intertropical Convergence Zone, leading to a tropical wet regime. In southern Africa, high-pressure cells lead to dry conditions and cause the existence of the Kalahari Desert (Mengistu and Mengistu Tsidu, 2020). Even though total annual precipitation is decreasing southwards, the whole region experiences distinct wet and dry seasons and is influenced strongly by the IAV in precipitation (Fan et al., 2015; Valentini et al., 2014). The study region is mainly covered by (woody) savannas, grassland, and shrubland (see Fig. 1).

The vegetation is mostly water limited in its growth (Williams et al., 2008) and exposed to large seasonal fires. The fire season starts in May in the western part of southern Africa and spreads eastwards to reach southern hemispheric Africa in September (Edwards et al., 2006). Fires on the whole African continent are the largest contributor to global fire carbon emissions, accounting for more than half of these emissions (van Marle et al., 2017; Shi et al., 2015; Valentini et al., 2014). They reduce the African carbon sink significantly (Lasslop et al., 2020). We subdivide the study region into a northern, savanna-dominated region and a southern grassland and shrubland region separated at 17° S, excluding Madagascar.

2.2 Total column CO_2 measurements

For our analyses, we use column-averaged dry-air mole fractions of CO_2 (XCO_2; referred to as CO_2 concentrations in the following) measured by the Greenhouse Gases Observing Satellite (GOSAT) over land in our study region. GOSAT was launched in 2009 and has a sub-satellite field of view of 10.5 km radius with a sparse sampling grid. We use GOSAT CO_2 concentration data generated by applying version 2.4.0 of the RemoTeC radiative transfer and retrieval algorithm (Butz, 2022), as used in Metz et al. (2023). The retrieval version covers the period from April 2009 to June 2019 and is based on the preceding RemoTeCv2.3.8, as used in Detmers et al. (2015). The major updates between versions 2.3.8 and 2.4.0 are stricter quality filtering in the latter and updated ancillary input data, especially for the prior gas concentrations used. Moreover, GOSAT CO_2 concentration data generated by version 9 of the NASA Atmospheric CO_2 Observations from Space (ACOS) algorithm (Lite), available for the period from April 2009 to June 2020, are used (Taylor et al., 2022). In the following, the datasets are called GOSAT/RemoTeC and GOSAT/ACOS (see Table A1 for more information about the datasets and the nomenclature used in this study). GOSAT/ACOS single measurements have a precision of 1.5 ppm and a mean bias of 0.2 ppm in validation against TCCON (Taylor et al., 2022). GOSAT/RemoTeC was found to have a similar precision of 1.9 ppm (Buchwitz et al., 2017) and, by construction, a mean bias of 0 ppm in comparison to TCCON after bias correction. GOSAT/RemoTeC was found to have regional and seasonal systematic errors of 0.6 and 0.5 ppm, respectively (Buchwitz et al., 2017).

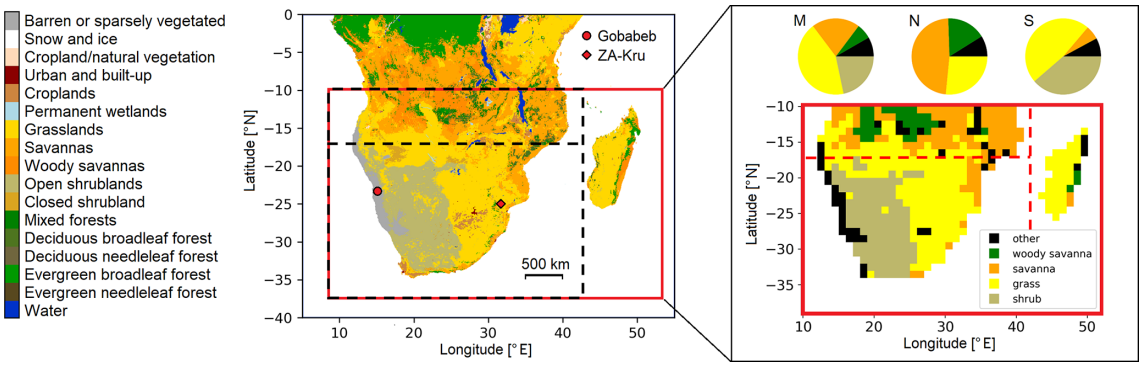

Figure 1. Study region southern Africa. The land cover in the study region is given based on MODIS (MCD12C1) data (Friedl and Sulla-Menashe, 2022). Additionally, the main region used for the analyses is depicted using a red box. In the inset map on the right-hand side, the land cover is aggregated into larger land cover classes and on a $1° \times 1°$ spatial resolution, which is used for most of the analyzed data. The main region, thereby, comprises 547 grid cells. The dashed boxes show the subdivision into a northern and a southern region. Madagascar is part of the main region, but it is excluded in the subdivision. The pie charts depict the share of the different land cover classes in the main study region (M), the northern subregion (N), and the southern subregion (S). The locations of the Gobabeb COCCON measurement site (Frey et al., 2021; Dubravica et al., 2021) and the flux tower in Kruger National Park (Archibald et al., 2009) are given as a red circle and red diamond, respectively.

For evaluation purposes, land glint and land nadir (LGLN) XCO_2 data (version 11.1r) measured by the Orbiting Carbon Observatory-2 (OCO-2) satellite are used (OCO-2/OCO-3 Science Team et al., 2022; Jacobs et al., 2024). OCO-2 was launched in 2014 and has a sub-satellite field of view of 1.3 km × 2.3 km. Furthermore, Collaborative Carbon Column Observing Network (COCCON) XCO_2 data from the Gobabeb station (Namibia; Frey et al., 2021; Dubravica et al., 2021) are taken for comparison. COCCON stations measure XCO_2 using a sun-viewing ground-based Fourier transform infrared spectrometer (Frey et al., 2019). We use the full dataset of COCCON measurements (i.e., we do not apply further filtering or co-sampling to GOSAT), as there are too few coinciding GOSAT measurements.

To examine the seasonal variability in CO_2 concentrations in the study region, the global background trend is subtracted from the total CO_2 measurements to obtain detrended CO_2 concentrations. For this, we assume a yearly linear increase in the global atmospheric CO_2 and use the annual mean CO_2 growth rate (GR) published by the National Oceanic and Atmospheric Administration (NOAA). The growth rates are based on globally averaged CO_2 concentration measurements of marine surface sites (NOAA, 2024); their calculation is further described in the main text and in Fig. A3 in Taylor et al. (2023) and in Pandey et al. (2024). The following equation describes the used background trend:

$$\mathrm{BG}_{y,m} = \mathrm{BG}_0 + \sum_{i=2009}^{y-1} (\mathrm{GR}_i) + \frac{m}{12}\mathrm{GR}_y. \quad (1)$$

Thereby, the increase in the CO_2 concentrations in the previous years from 2009 onwards is described by the second part in the equation. The increase within the previous months in the respective year is given by the third part. Both are added to an overall offset BG_0 in 2009. This offset is estimated so that the mean of the detrended CO_2 concentrations over the whole time period is zero.

2.3 Fluxes

2.3.1 Top-down fluxes

Carbon fluxes can be obtained by assimilating measured CO_2 atmospheric concentrations in an atmospheric inversion. Atmospheric inversions typically build on Bayesian optimization (i.e., they optimize forward-transported CO_2 emissions such that these agree best with the observations within measurement and model uncertainties, while concurrently not deviating from the prior within given prior uncertainties). For our study, we use three atmospheric inversions based on in situ CO_2 measurements: the TM5 four-dimensional variational inversion system (TM5-4DVar; Basu et al., 2013), NOAA's modeling and assimilation system CarbonTracker (CT2022; Peters et al., 2007; Jacobson et al., 2023), and the Copernicus Atmosphere Monitoring Service (CAMS; Chevallier et al., 2005, 2010, 2019). The models estimate global CO_2 fluxes based on a set of in situ CO_2 measurements from global monitoring networks (Masarie et al., 2014). The models use different prior datasets. For example, for the biogenic CO_2 fluxes, TM5-4DVar and CarbonTracker build on different implementations of the Carnegie–Ames–Stanford approach (Randerson et al., 1996), as further described in Metz et al. (2023), Weir et al. (2021), and Jacobson et al. (2023), while CAMS uses biogenic fluxes of the ORCHIDEE model (Chevallier et al., 2019). Furthermore, the inversion systems use different transport models and inversion techniques. While TM5-4DVar and CarbonTracker use the TM5 transport model, CAMS uses the LMDZ global atmospheric transport model. TM5-4DVar and

CAMS make use of a 4DVar data assimilation, while CarbonTracker uses an ensemble Kalman filter. All three models use ECMWF ERA5 data as meteorological drivers. The output resolution is monthly at $3° \times 2°$ for TM5-4DVar and CarbonTracker2022 and monthly at $3.7° \times 1.81°$ for CAMS (see Table A1 for more details). The ensemble of the three models is referred to as "in-situ-only" inversions in the following, while TM5-4DVar based on in situ measurements is called "TM5-4DVar/IS".

In addition to in situ measurements, satellite CO_2 concentration measurements can be assimilated by atmospheric inversions. To this end, we use the TM5-4DVar model and assimilate GOSAT CO_2 concentration measurements over land and ocean as well as the in situ measurements. We use the individual total CO_2 concentration measurements; i.e., we do not apply any detrending or spatiotemporal averaging. Detrending and spatiotemporal averaging is only applied for visualization purposes to show the variability in the monthly CO_2 concentrations (Sect. 3.1). Depending on the specific GOSAT dataset used, we refer to these fluxes in the following as "TM5-4DVar/RemoTeC + IS", "TM5-4DVar/ACOS + IS", or (when using the mean of both) "TM5-4DVar/GOSAT + IS". More details about the TM5-4DVar settings can be found in Metz et al. (2023). For comparison, we also draw on data of the OCO-2 Model Intercomparison Project (MIP; Byrne et al., 2023) for the years from 2015 to 2018. Within the MIP, atmospheric inversions estimate carbon fluxes by assimilating OCO-2 satellite XCO_2 observations and in situ data. All MIP inversion models use the same fossil fuel emission dataset but differ with respect to the chosen datasets for all other prior fluxes (Byrne et al., 2023). We specifically make use of the LNLGIS (assimilation of OCO-2 LNLG observations and in situ measurements) and the IS (assimilation of in situ measurements only) experiment in the following, referred to as "MIP/OCO-2 + IS" and "MIP/IS", respectively. Like Byrne et al. (2023), we exclude the LoFI MIP model, as it uses a nontraditional inversion scheme differing from the MIP protocol. MIP/OCO + IS and MIP/IS provide fluxes with a monthly, $1° \times 1°$ resolution.

All inversions optimize for biogenic and oceanic fluxes but impose anthropogenic fossil fuel emissions and fire emissions. The sum of (imposed) fire and biogenic fluxes yields our net biome productivity (NBP) estimates. In this study, positive fluxes denote a release of CO_2 from land into the atmosphere. All fluxes are regridded to monthly, $1° \times 1°$ fluxes before performing the region selection.

By transporting the posterior fluxes after the optimization, atmospheric inversions can model posterior concentration fields, which can be interpolated to the time and location of the satellite measurements for comparison. This so-called co-sampling is used to eliminate sampling errors when comparing modeled concentrations to satellite measurements. We use the modeled and co-sampled posterior concentrations of the in-situ-only inversions introduced at the beginning of this section.

2.3.2 Bottom-up fluxes

We compare the top-down CO_2 fluxes to bottom-up flux datasets from DGVMs as collected by version 9 of the "Trends and drivers of the regional-scale terrestrial sources and sinks of carbon dioxide" (TRENDY; Le Quéré et al., 2013; Sitch et al., 2020) intercomparison project. The project was established to support the annual global carbon budget estimation conducted by the Global Carbon Project (e.g., Friedlingstein et al., 2020). These TRENDY models give vegetation CO_2 fluxes simulated using a harmonized set of meteorological input data and CO_2 concentrations (Le Quéré et al., 2013; Friedlingstein et al., 2020). We use the NBP, gross primary productivity (GPP), autotrophic respiration (RA), and heterotrophic respiration (RH) of 18 DGVMs (see Table A1 in the Appendix). We thereby use the following definition:

$$\begin{aligned} \mathrm{NBP} &= \mathrm{NEE} + \mathrm{fire} + \mathrm{fluc} = \mathrm{TER} - \mathrm{GPP} + \mathrm{fire} + \mathrm{fluc} \\ &= \mathrm{RH} - \mathrm{NPP} + \mathrm{fire} + \mathrm{fluc}, \end{aligned} \tag{2}$$

with the total ecosystem respiration (TER), calculated as the sum of RA and RH; the fire emissions (fire); the land use change fluxes (fluc); and the net primary productivity (NPP), calculated as the GPP minus the RA. Most of the TRENDY models provide NBP fluxes directly. In the case of the CABLE-POP and DLEM models, NBP is calculated as RH minus NPP, as both models do not provide fire and land use change fluxes. The spatial resolutions of the model output differ (see Table A1). Therefore, we aggregate fluxes on a monthly, $1° \times 1°$ grid before applying the region selection.

Additionally, we use version 1 (setup RS_V006) of the FLUXCOM net ecosystem exchange (NEE) product, as described in Jung et al. (2020). FLUXCOM uses machine learning models and meteorological data to upscale eddy-covariance tower CO_2 flux measurements to the global scale (Tramontana et al., 2016; Jung et al., 2020). To obtain an NBP estimate, we combine the NEE fluxes with fire CO_2 emissions provided by the Global Fire Emissions Database (GFED; van der Werf et al., 2017). FLUXCOM and GFED are provided as $0.08° \times 0.08°$, 8 d fluxes and $0.25° \times 0.25°$, daily fluxes, respectively, and are aggregated on a monthly, $1° \times 1°$ grid before applying the region selection.

2.4 Other datasets

To investigate the climatic conditions influencing the carbon fluxes, we use temperature, upper-layer soil moisture, and precipitation datasets of the European Centre for Medium-Range Weather Forecasts (ECMWF) ERA5-Land data product (Muñoz Sabater, 2019) with a monthly resolution on a $0.25° \times 0.25°$ spatial grid. ERA5 datasets are aggregated on a $1° \times 1°$ grid before performing the region selection. Fur-

thermore, we use solar-induced fluorescence (SIF) measurements by the GOME-2 satellite from 2009 to January 2018 (Joiner et al., 2023). SIF is considered to be proportional to GPP on a monthly timescale and at a biome resolution (Sun et al., 2018; Joiner et al., 2018; Pierrat et al., 2022; Zhang et al., 2016a, b). It can, therefore, be used as a proxy for CO_2 uptake by photosynthesis (Li et al., 2018).

3 Results

3.1 Monthly CO_2 concentrations by atmospheric inversions

To access the seasonal and interannual dynamics in southern Africa, we detrend the monthly mean CO_2 concentrations following Eq. (1) (see Sect. 2.2). The remaining CO_2 enhancements for the study region are shown in Fig. 2. The GOSAT-measured CO_2 enhancements reveal a clear seasonal cycle with a minimum concentrations in the first half of the year and maximum concentrations in the second half of the year. This general seasonal timing is confirmed by the posterior concentrations of the in-situ-only inversions. However, yearly reoccurring differences between GOSAT and the in-situ-only based CO_2 enhancements from September to November are clearly visible. Thus, the spread between GOSAT/ACOS and GOSAT/RemoTeC (see also Fig. A1) is much smaller than their difference from and the spread among the in-situ-only inversions. The difference pattern between GOSAT and in-situ-only-based CO_2 concentrations has already been described by Mengistu and Mengistu Tsidu (2020) and has been shown by Taylor et al. (2022). Furthermore, especially in the second half of the year, different in-situ-only inversions are not consistent, as indicated by the large shading in Fig. 2a (see also the individual models in Fig. A2). Reasons for these discrepancies will be further analyzed in Sect. 3.3.

For comparison, we additionally use the OCO-2 satellite, which was launched in 2014, and 1 year of COCCON CO_2 column measurements in Namibia. Both datasets show a similar seasonal cycle to that seen by GOSAT; i.e., they show concentration maxima later in the year than the in-situ-only inversions (see Figs. A3 and A4). No other total column measurement sites – e.g., of the COCCON network or Total Carbon Column Observing Network (TCCON, Wunch et al., 2011) – with coinciding consecutive measurements for more than 1 year exist in the Southern Hemisphere for continental Africa, limiting the validation possibilities of satellite total column measurements in this region.

3.2 Southern African top-down and bottom-up CO_2 fluxes

Assimilating the GOSAT CO_2 concentration measurements in TM5-4DVar, we obtain GOSAT-based top-down fluxes at a monthly resolution for the study region (see Sect. 2.3.1). As for the concentrations, a clear seasonal cycle is visible (Fig. 3). From January to May, CO_2 is taken up by the land surface, with a maximum uptake around March. From June to December, CO_2 is released into the atmosphere and reaches a maximum flux in September to November. The number of GOSAT measurements (see Figs. A5 and A6) is variable throughout the year, with the smallest number occurring during the rainy season around December and January. This leads to larger uncertainties in the monthly mean satellite CO_2 concentrations and satellite-based fluxes during the transition from maximum to minimum concentrations and fluxes.

A similar timing of the seasonal cycle is also captured by the in-situ-only inversion fluxes (CAMS, CT2022, and TM5-4DVar/IS). However, the in-situ-only inversions' seasonal amplitude is smaller than for TM5-4DVar/GOSAT + IS. To analyze the differences found between TM5-4DVar/GOSAT + IS and the in-situ-only atmospheric inversions, we evaluate the information content provided by the measurements about the southern African carbon fluxes. To this end, we compare the TM5-4DVar fluxes (TM5-4DVar/IS and TM5-4DVar/GOSAT + IS) to the prior fluxes of the inversion model. From Fig. 4, it becomes clear that the in-situ-only fluxes (TM5-4DVar/IS) mainly follow the dynamics of the prior fluxes, whereas the GOSAT-based fluxes deviate significantly from the prior. This is expected, as the sparse coverage of in situ measurements in Africa (and the Southern Hemisphere in general) provides only little information about the African carbon fluxes. In contrast, satellites provide nearly global coverage of CO_2 measurements. Using these measurements in TM5-4DVar, new information about the southern African carbon fluxes can be obtained and may lead to a deviation of TM5-4DVar/GOSAT + IS from the prior. This finding also explains the differences among the three in-situ-only inversions (see shaded range of the in-situ-only inversions in Fig. 3). The inversions assume different prior fluxes, which they follow closely, as the information from the in situ data does not substantially inform the inversion.

When assimilating OCO-2 satellite measurements instead of GOSAT measurements, the MIP/OCO-2 + IS ensemble mean also shows a larger amplitude of the southern African carbon fluxes compared with in-situ-only inversions and MIP/IS (Fig. 5). However, the spread among the MIP/OCO-2 + IS models is large, especially during the maximum emissions from September to November. Some models show lower emissions similar to the in-situ-only inversions, whereas others agree with TM5-4DVar/GOSAT + IS. By analyzing the performance of the individual models in these 3 months, we find that three MIP/OCO-2 + IS models reproduce the OCO-2 measurements the best (see Fig. A7), indicating that the OCO-2 measurements were given a considerable weight in the inversion and, thus, that the optimized fluxes were informed by measurements (see Appendix A). At the same time, these three inversion models (Baker, CAMS,

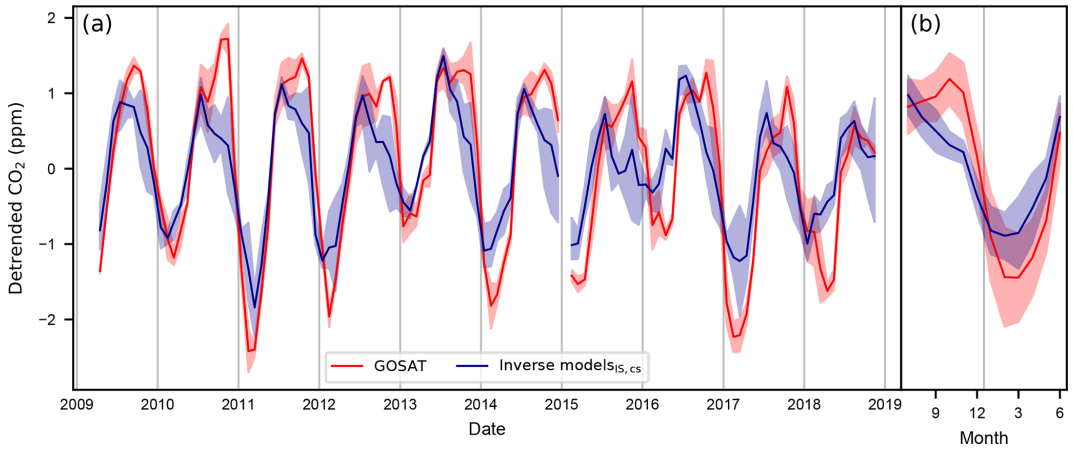

Figure 2. Monthly southern African detrended CO_2 concentrations. GOSAT-measured and detrended CO_2 concentrations are depicted in red. Modeled posterior CO_2 concentrations of three in-situ-only inversions are co-sampled (cs) on GOSAT and depicted as the mean (in blue). Panel **(a)** shows the monthly mean CO_2 concentrations. The shading indicates the range among the individual ensemble members (GOSAT/ACOS + IS and GOSAT/RemoTeC + IS in red; CT2022, CAMS, and TM5-4DVar/IS in blue). Panel **(b)** shows the mean seasonal cycle for 2009–2018, with the standard deviation over the years given as shading.

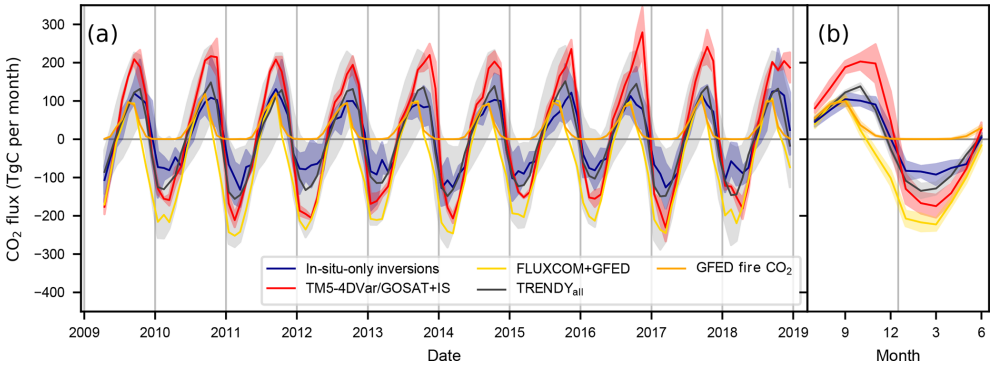

Figure 3. Top-down and bottom-up southern African net CO_2 fluxes. Panel **(a)** shows the mean monthly net CO_2 fluxes for the southern African region, while panel **(b)** shows the mean seasonal cycle of the fluxes over the 2009 to 2018 period. The TM5-4DVar/GOSAT + IS fluxes are given in red, whereas in-situ-only inversion fluxes are shown in blue. The mean over all TRENDY models is given in gray. GFED fire emissions are shown in orange, whereas they are displayed in combination with FLUXCOM NEE in yellow. The shading indicates the range over the GOSAT-based fluxes (TM5-4DVar/ACOS + IS and TM5-4DVar/RemoTeC + IS) and the in-situ-only inversion fluxes (CT2022, CAMS, and TM5-4DVar/IS) and the standard deviation over the TRENDY ensemble in panel **(a)**. In panel **(b)**, shading indicates the standard deviation over the years. Positive fluxes indicate emissions into the atmosphere. Negative fluxes correspond to an uptake of CO_2 into the land surface.

and TM5-4DVar/OCO-2 + IS) show the largest CO_2 emissions and agree best with TM5-4DVar/GOSAT + IS (see Figs. 5 and A7–A9). Still, their estimated emissions are slightly lower than those of TM5-4DVar/GOSAT + IS. When directly comparing the two TM5-4DVar inversions TM5-4DVar/GOSAT + IS and TM5-4DVar/OCO-2 + IS (Fig. 5), the latter has smaller emission values. This is most likely a result of the slightly smaller seasonal amplitude of the CO_2 concentrations measured by OCO-2 compared with GOSAT (see Fig. A3).

In conclusion, we find that satellite-based inversions, which are actually compatible with the satellite measurements, show larger carbon fluxes in southern Africa than in-situ-only inversions, which suffer from the limited information provided by the sparse in situ measurements for southern Africa. Our results support current studies (e.g., Basu et al., 2013; Sellers et al., 2018; He et al., 2023) reporting that satellite observations do inform atmospheric inversions well for flux estimates at subcontinental scales. Satellite CO_2 concentration measurements, therefore, provide a unique information source and are especially valuable in regions with sparse in situ measurement coverage. The already long record provided by GOSAT will be more and more complemented over time by the growing record of OCO-2 and future CO_2 sensors providing even more extensive measurements.

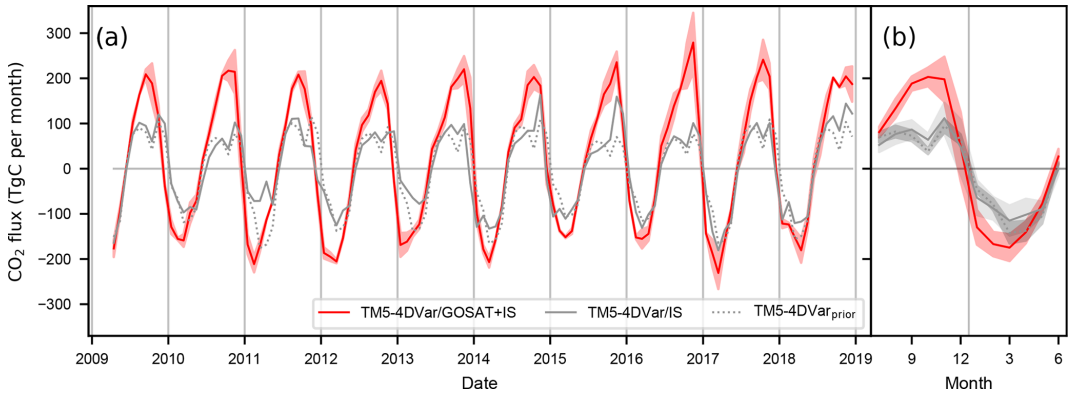

Figure 4. Top-down southern African net CO_2 fluxes from TM5-4DVar. In panel **(a)**, mean monthly net CO_2 fluxes for the southern African region from the TM5-4DVar prior (dotted gray line), the in-situ-only inversion TM5-4DVar/IS (solid gray line), and the TM5-4DVar/GOSAT + IS inversion (solid red line) are given. Red shading indicates the range of the TM5-4DVar/ACOS + IS and TM5-4DVar/RemoTeC + IS inversions. Panel **(b)** shows the mean seasonal cycle for 2009–2018, with the standard deviation over the years given as shading.

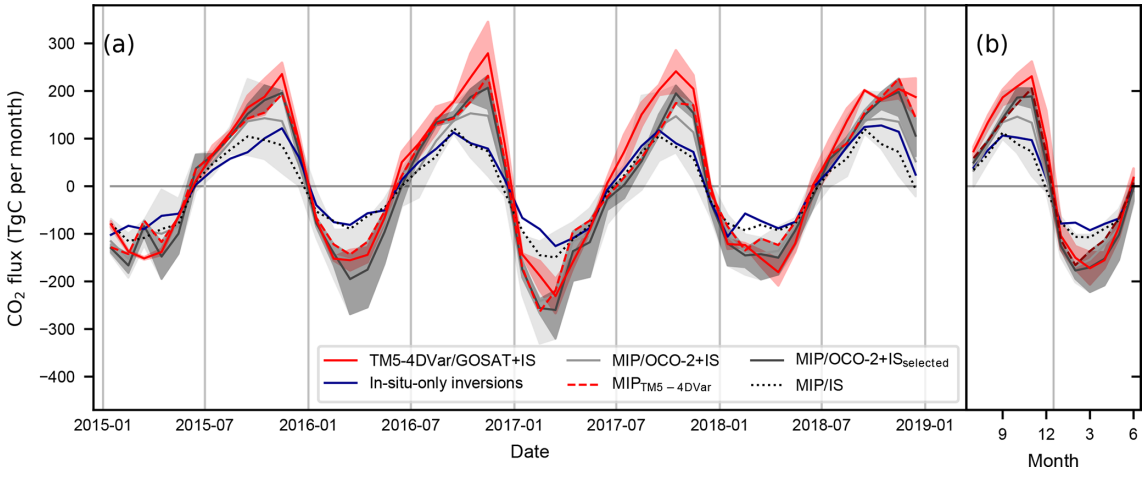

Figure 5. Top-down southern African net CO_2 fluxes from MIP. In panel **(a)**, mean monthly net CO_2 fluxes for the study region are given by TM5-4DVar/GOSAT + IS (solid red line), the MIP/OCO-2 + IS ensemble mean (solid gray line), the mean over three selected MIP models (CAMS, TM5-4DVar, and Baker; solid black line), and TM5-4DVar/OCO-2 + IS as part of the MIP ensemble (dashed red line). In-situ-only inversion fluxes are given as a solid blue line for the mean of CAMS, CT2022, and TM5-4DVar/IS, whereas they are given as a dotted black line from the MIP/IS ensemble. The shading indicates the range over the GOSAT fluxes (TM5-4DVar/ACOS + IS and TM5-4DVar/RemoTeC + IS), the MIP ensemble, and the three selected MIP models. Panel **(b)** gives the mean seasonal cycle from 2015 to 2018, with shading indicating the range over the MIP ensembles' models and the standard deviation of the TM5-4DVar/GOSAT + IS over the years.

Next to the in-situ-only inversion fluxes, we compare the TM5-4DVar/GOSAT + IS fluxes to FLUXCOM CO_2 fluxes. As FLUXCOM only provides NEE fluxes, we add GFED fire CO_2 emissions to obtain an NBP estimate. In Fig. 3, FLUXCOM + GFED only reaches positive monthly fluxes from June to September due to fire emissions occurring during that time. From October to May, it shows a net CO_2 uptake. While the timing of the maximum sink agrees well between FLUXCOM + GFED and the inversion fluxes, FLUXCOM + GFED shows a smaller amplitude and an earlier drop in emissions compared with TM5-4DVar/GOSAT + IS and in-situ-only inversion fluxes. The tendency of FLUXCOM to report a stronger carbon sink for the Southern Hemisphere compared with other datasets is described in Jung et al. (2020). It is expected that the sparsity of eddy-covariance towers in Africa or in similar ecosystems hampers the machine-learning-based approach of FLUXCOM for estimating CO_2 fluxes in the study area. Jung et al. (2020) described larger uncertainties due to representation errors in semiarid regions.

Finally, we compare the inversion results to the ensemble of process-based vegetation models of the TRENDYv9

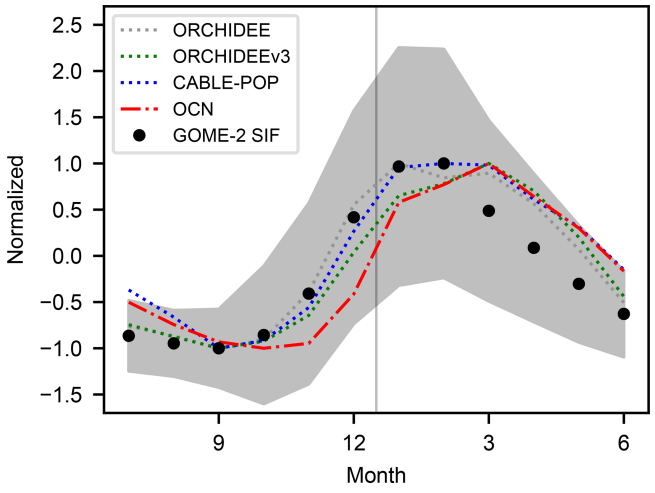

Figure 6. Seasonal cycle of SIF and selected TRENDY models. The normalized mean seasonal cycles of GOME-2 SIF (2009–January 2018), GPP from the three selected DGVMs (ORCHIDEE, ORCHIDEEv3, and CABLE-POP), and OCN GPP (2009–2018) are shown using solid black symbols, colored dotted lines, and a red dot-dash line, respectively. The spatial standard deviation over monthly GOME-2 SIF aggregated to $1° \times 1°$ is given as shading.

project. The mean of the DGVM ensemble in Fig. 3a shows a smaller amplitude than the GOSAT fluxes and compares with the in-situ-only inversion fluxes. However, as indicated by the large standard deviation, the models deviate substantially from each other. Foster et al. (2024) and Metz et al. (2023) observed a similar large spread among DGVMs for the North American temperate region and Australia, respectively. Both studies highlight the importance of performing a sub-selection of DGVMs agreeing well with atmospheric CO_2 measurements.

3.3 GOSAT and SIF atmospheric constraints on TRENDY models

Given the large spread of the TRENDY models, we select DGVMs according to their agreement with the GOSAT-based CO_2 fluxes and SIF. Thus, in a first step, we compare the monthly mean DGVM and TM5-4DVar/GOSAT + IS NBP and NEE fluxes based on the root-mean-square error (RMSE) of the monthly fluxes and the agreement in the seasonality. In a second step, only for the well-matching DGVMs, we additionally compare the GPP normalized mean seasonal cycle to the GOME SIF normalized mean seasonal cycle. Only models with a timing of the minimum and maximum GPP agreeing within ±1 month with the normalized SIF seasonal cycle are selected (see Fig. 6). This ensures the correct seasonal timing of the modeled GPP fluxes.

Based on these criteria, we select the ORCHIDEE (RMSE NBP: 60.2 TgC per month; RMSE NEE: 68.2 TgC per month), ORCHIDEEv3 (RMSE NBP 70.2 TgC per month; RMSE NEE: 56.2 TgC per month) and CABLE-POP (RMSE NBP: 78.2 TgC per month; RMSE NEE: 63.6 TgC per month) models. All other models, except for the model OCN, had already been excluded in the first step of the NBP and NEE comparison. OCN performs well in the NBP and NEE comparison but shows larger deviations in the SIF–GPP comparison (see Fig. 6). Therefore, it was excluded in the second selection step and is not included in the TRENDY selection. The exclusion of OCN underlines the importance of the SIF/GPP selection and demonstrates that a correct timing of the net CO_2 exchange fluxes does not necessarily imply the correctness of the modeled gross fluxes. In general, it is noteworthy that only 3 out of 18 TRENDY models pass our selection process. This again reveals the large uncertainties associated with the TRENDY ensemble estimate for semi-arid southern Africa.

The NBP mean over these three models is given in Fig. 7a and b. The models reproduce the timing and strength of the TM5-4DVar/GOSAT + IS NBP fluxes. Only at the beginning of the emission period around July to September are the TRENDY selection fluxes lower. Furthermore, the selection shows a significantly smaller sink in 2012 and a smaller source in 2016. Note that ORCHIDEE is part of the TRENDY selection and is also used by the in-situ-only inversion CAMS as prior flux assumption. This explains why CAMS best matches TM5-4DVar/GOSAT + IS CO_2 fluxes and GOSAT CO_2 concentrations (see Figs. A2 and A7, respectively).

Fire emissions contribute substantially to the seasonality in the southern African carbon fluxes. They largely explain the beginning of the emission period from July to September (see Fig. 3). Different fire emission data products differ significantly and suggest large uncertainties in the magnitude of the actual fire emissions in our study region (see Fig. A10). GFED, which we use for our analyses, shows the largest fire emissions but could even underestimate the actual emissions as suggested by current literature for southern hemispheric Africa (Ramo et al., 2021; van der Velde et al., 2024).

To exclude the influence of fire emission in the comparison, we analyze the monthly NEE fluxes of the TRENDY selection compared with the TM5-4DVar/GOSAT + IS NBP fluxes with GFED fire emissions subtracted. The subtraction of the fire emissions leads to a better agreement between both datasets, especially at the beginning of the emission period, suggesting that fire fluxes in the DGVMs do not agree with the GFED fire fluxes (see Fig. 7c and d). This goes along with the large uncertainties in DGVM fire fluxes reported previously (Bastos et al., 2020).

Figure 7c additionally shows the annual NEE fluxes (July–June) as bars. The absolute difference between TM5-4DVar/GOSAT + IS and TRENDY annual fluxes is large in some years. These differences are caused by a stronger sink at the beginning of 2012 and enhanced emissions at the end of 2013 and 2016 in TM5-4DVar/GOSAT + IS compared with TRENDY. However, while both datasets do not agree on the absolute value of annual fluxes in most of the years, they

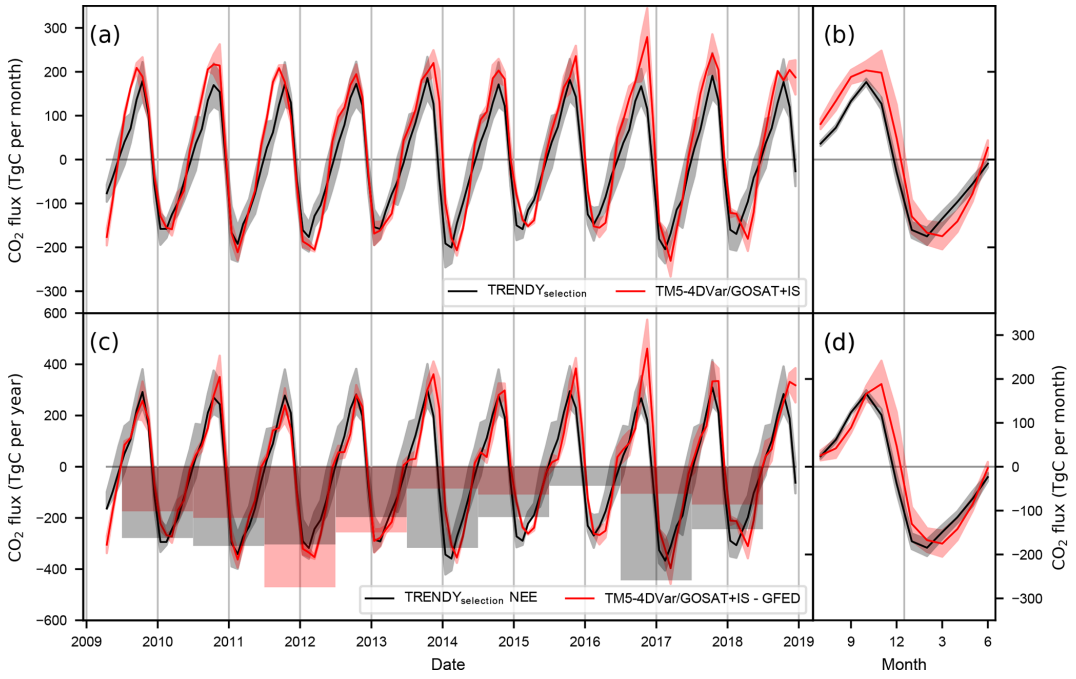

Figure 7. Annual and mean monthly NBP and NEE fluxes in southern Africa. The NBP fluxes from TM5-4DVar/GOSAT + IS (red) and selected TRENDY models (black) are given as mean monthly fluxes in panel **(a)** and as the mean seasonal cycle in panel **(b)**. Similar to that, panels **(c)** and **(d)** show the monthly NEE fluxes (GFED is subtracted from TM5-4DVar/GOSAT + IS). Additionally, the annual (July–June) NEE fluxes of the selected TRENDY models and TM5-4DVar/GOSAT + IS–GFED fluxes are given. The shading indicates the standard deviation over the TRENDY models and the range of TM5-4DVar/ACOS + IS and TM5-4DVar/RemoTeC + IS in panels **(a)** and **(c)** and the standard deviation of the monthly fluxes over the years in panels **(b)** and **(d)**.

show a similar IAV. Both datasets show a slightly stronger CO_2 uptake from 2010 to 2012. These years were strong and moderate La Niña years with enhanced rainfall in 2010 and 2011 in the study region compared with the long-term mean (see Fig. A11). Additionally, lower-than-average temperatures led to enhanced soil moisture near the surface in 2010–2011. The soil moisture declined in 2012 to reach the long-term average. In 2015 and 2016, the sink given by the GOSAT and TRENDY selection NEE fluxes is small. These 2 years were a weak and a strong El Niño year, respectively, with dry conditions and, in the case of 2016, exceptionally high temperatures (see Fig. A11). These findings agree well with the results of Pan et al. (2020), who highlighted the fact that temperature and precipitation extremes heavily impact African ecosystems and, therefore, play a key role in the African carbon fluxes.

To conclude, the monthly NEE and NBP fluxes and, to a lesser extent, the IAV in the selected TRENDY models agree well with TM5-4DVar/GOSAT + IS NEE and NBP, although the latter was not a criterion in the selection process of the TRENDY models. This suggests that the selected models indeed capture the carbon cycle dynamics, even on a decadal timescale. For this reason, we use the model selection for further investigations of the vegetation processes driving the southern African carbon cycle.

3.4 Seasonal and interannual variability in TRENDY gross fluxes

To investigate the vegetation dynamics shaping the seasonal cycle of the southern African CO_2 exchange, we use the selected TRENDY models to further split up the net ecosystem exchange fluxes into the gross fluxes NPP (GPP − RA) and RH. The gross and net fluxes are given as the mean seasonal cycle and annual anomalies in Fig. 8. In the mean seasonal cycle for the whole study region (Fig. 8a), we can see a clear difference in timing between RH and GPP − RA. Heterotrophic respiration increases early in September and October, while RA increases 1–2 months later along with GPP (see Fig. A12). The dephasing between RH and GPP − RA leads to a prolonged emission phase in the net CO_2 exchange. It takes place in the whole region and occurs in the savanna-dominated north (Fig. 8c) and in the grassland and shrublands in the south (Fig. 8e). The dephasing takes place in every year (see Fig. A13) and is present in all selected TRENDY models. It causes a mean CO_2 release of 494 TgC during the emission phase, which is about 17 % and 18 % of the annual total RH and GPP − RA, respectively. When looking at the monthly precipitation over the study region (see Fig. A14), one can identify a distinct drought phase occurring in the whole study region. The subsequent start of the

rainy season in September and October temporally coincides with the early increase in RH. This finding resembles the results of Metz et al. (2023) in Australia: an increase in soil respiration with the beginning of the rainy season prior to the start of the growing season. Their study found soil respiration pulses resulting from the rewetting of soils to cause the continental-scale increase in soil respiration. Such soil respiration pulses at local arid sites are discussed in the context of the Birch effect (Birch, 1964; Jarvis et al., 2007), whereby the rewetting of the soil enables microbial populations to grow and to transform the carbon stored in the soils into CO_2 emissions. CO_2 is then released in substantial amounts within a short period of time. As in Metz et al. (2023), we find short-duration emission pulses in the daily flux record of a FLUXNET station in the study region. Exemplary annual records of the FLUXNET station in the Kruger National Park (Archibald et al., 2009) show CO_2 emission caused by precipitation pulses (see Fig. A15). This is also reported in Fan et al. (2015), who studied a 2-year measurement record of carbon fluxes in Kruger National Park in more detail. Their study found recurring respiration emission pulses due to precipitation events and attributed them to the Birch effect. The TM5-4DVar/GOSAT + IS fluxes indicate an even larger time lag between the increase in soil respiration and NPP in some years compared with TRENDY. A prolonged emission phase of an additional 1–2 months (see Fig. 7c) takes place in years with especially low soil moisture (2013, 2015, and 2016; see Fig. A11). This later drop in emissions could either be caused by a delayed start of the GPP rise in the growing season or enhanced soil respiration due to the drier conditions causing an enhanced accumulation of soil carbon during the years. It is not possible to investigate this further, as none of the TRENDY DGVMs captured the IAV in the timing of the emission phase.

It is noteworthy that large parts of the unselected "other" TRENDY models miss the dephasing between RH and GPP − RA. Their NBP estimates, therefore, do not agree with the emissions around October found by the satellite inversion. Implementing soil respiration due to rewetting more accurately in those models could improve their agreement with the satellite-based fluxes. Metz et al. (2023) found that the dephasing in the TRENDY models is most likely caused by a different response time of soil respiration and vegetation growth to precipitation; e.g., water needs to percolate into the deeper soil layers with plant roots to initiate plant growth, whereas heterotrophic respiration is driven by upper-soil-layer soil moisture or precipitation. The implementation of such a time lag between heterotrophic respiration and GPP seems to be a necessary but not a sufficient prerequisite to accurately capture the seasonal carbon flux variability in semiarid southern Africa. Our results call for studies on how to implement the response of ecosystems to soil rewetting more accurately to improve the consistency and accuracy of the TRENDY ensemble in semiarid regions.

Looking at the annual gross flux anomalies given by the TRENDY selection (Fig. 8b), we see that the IAV in NBP and NEE is mainly driven by GPP. Enhanced GPP from 2010 to 2012 leads to a constantly stronger uptake of CO_2. In 2017, a strongly enhanced GPP causes a large CO_2 sink. Reduced GPP in 2013, 2015, and 2016 results in positive NEE anomalies associated with a reduced NEE sink. RH only plays a minor role and mostly slightly counteracts the GPP anomalies. These findings agree with the studies of Ciais et al. (2009), Weber et al. (2009), and Williams et al. (2008), who identified GPP variability as a major source of African fluxes' IAV. It is, however, in contrast to semiarid Australia, where Metz et al. (2023) found a large IAV in RH driven by precipitation anomalies during the dry season. The African study region, however, has a distinct and regular dry season every year (see Fig. A14), leading to a smaller influence of RH on the IAV. Note that GOSAT suggests a much smaller annual CO_2 sink in 2017. However, the discrepancy is mainly caused by a significant difference in the emissions in the second half of the year, while both datasets agree well with respect to the phase of carbon uptake (see Fig. 7c). Therefore, the TM5-4DVar/GOSAT + IS fluxes support the large GPP anomaly given by the TRENDY models but suggest stronger respiration or fire fluxes at the end of 2016.

Looking at the subregions (Fig. 8d and f), one can see that the sinks in 2010, 2011, and 2017 are mainly driven by the southern grassland region, where enhanced precipitation occurred during these years (see Fig. A11). The comparably large release in 2016 seems to be driven by the whole African region experiencing the highest annual temperatures and driest conditions within the 10-year study period. Therefore, the GPP IAV seems to be heavily impacted by precipitation variability. According to GFED (see Fig. A10), fire emissions play a minor role in impacting GPP and driving NBP anomalies. The variability in fire emissions is much lower than for NBP and GPP − RA. In the whole study region, the IAV (calculated as standard deviation over the years) in the GPP − RA and NBP fluxes is 97.7 and 94.1 $TgC\,yr^{-1}$, respectively. The IAV in GFED fire emissions is 27.3 $TgC\,yr^{-1}$, which is a similarly low value to the IAV in RH (27.1 $TgC\,yr^{-1}$). Furthermore, the annual fire emissions do not amplify the trend in the NBP anomalies. They were at a normal level during the large positive NBP anomaly in 2016. Higher-than-average fire emissions counteract the sink anomalies in 2011–2012, and only the slightly reduced fires in 2017 amplify the sink anomaly.

4 Conclusions

The sparsity of in situ CO_2 concentration and flux measurements results in large uncertainties in carbon flux estimates in the southern African region. We show that satellite measurements provide additional information, leading to an improvement in our knowledge about the southern African carbon

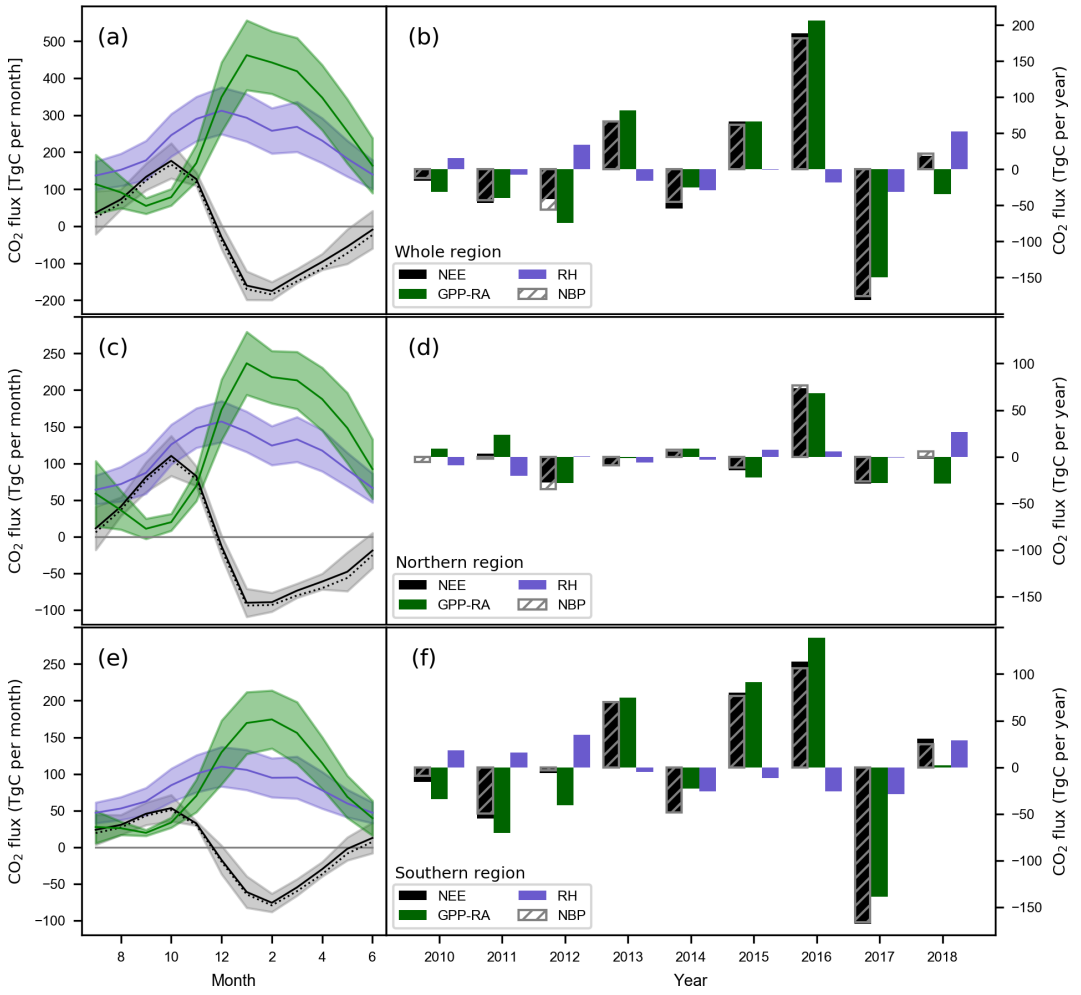

Figure 8. Annual and mean monthly CO_2 net and gross fluxes. The mean monthly fluxes **(a, c, e)** and annual (July–June) anomalies **(b, d, f)** of NEE, NBP, GPP − RA, and RH of the selected TRENDY models are given in black, gray (dotted), green, and blue, respectively. The fluxes are given for the whole study region **(a, b)**, the savanna-dominated northern region (north of 17° S; **c, d**), and the southern region with grassland and shrubland **(e, f)**. The annual anomalies are calculated by subtracting the individual long-term mean of the annual fluxes. Thus, a positive GPP anomaly denotes a reduced GPP and vice versa. The shading in panels **(a)**, **(c)**, and **(e)** indicates the standard deviation over the three selected models (ORCHIDEE, ORCHIDEEv3, and CABLE-POP).

cycle. Our study demonstrates that satellite-measurement-based atmospheric inversions and SIF can be used as atmospheric constraints for sub-selecting TRENDY DGVMs. This is necessary, as TRENDY flux estimates show a large spread in our study region.

Using the satellite-based selection of TRENDY DGVMs, we find that the IAV in NBP and NEE in southern Africa is driven by GPP variability. This supports findings by Ciais et al. (2009), Weber et al. (2009), and Williams et al. (2008) using individual vegetation models. The enhancements in annual GPP mainly originate in the grasslands and shrublands in the southern part of the study region and occur in years with an enhanced amount of precipitation. The seasonal variability in the southern African carbon fluxes is impacted by soil respiration dynamics, which are driven by the onset of the rainy season. Respiration pulses have been reported under the term of the Birch effect for arid Africa (Fan et al., 2015) and have been shown to be relevant at the continental scale in semiarid Australia (Metz et al., 2023). This enforces the relevance of rain-induced CO_2 emissions for the southern African region and for semiarid regions in general. Our results emphasize the importance of correctly representing the response of semiarid ecosystems to soil rewetting in DGVMs (e.g., different response times of RH and GPP), as this was found to be a prerequisite to accurately capture the seasonal carbon cycle dynamics.

Appendix A: The performance of the individual MIP models.

In Fig. 5, the ensemble mean of MIP/OCO-2 + IS shows lower emissions than TM5-4DVar/GOSAT + IS in the second half of the year. A selection of three models (Baker, TM5-4DVar, and CAMS), however, shows larger fluxes and agrees better with the GOSAT-based fluxes (see Sect. 3.2 and Fig. 5). Next to the OCO-2-informed posterior fluxes used for the analysis in the main text, the MIP/OCO-2 + IS dataset provides the prior fluxes used by the individual MIP models. Furthermore, 5 % of the OCO-2 measurements are withheld for validation purposes and modeled XCO_2 values co-sampled on the left-out measurements are provided for each model except CSU. The OCO-2 co-samples and the prior fluxes of the MIP models can be used to further evaluate the differences between the three selected models and the other MIP models.

In Fig. A7, the mismatch between XCO_2 modeled by the MIP and XCO_2 measured by OCO-2 is given for the months of the strongest emissions (September–November). The XCO_2 mismatch is the smallest for the three selected models, Baker, TM5-4DVar, and CAMS, which concurrently have the smallest mismatch to TM5-4DVar/GOSAT + IS. Hence, the models that reproduce the OCO-2 measurements best also agree best with the GOSAT-based CO_2 fluxes.

The differences between posterior and prior fluxes for the MIP models are given in Fig. A8. TM5-4DVar and Baker have the largest differences between the posterior and prior fluxes. Therefore, it is likely that, even though the prior fluxes of TM5-4DVar and Baker deviate strongly from the GOSAT-based fluxes (see Fig. A9), considerable weight was given to the OCO-2 measurements in the inversion. As a result, the posterior fluxes are closer to the GOSAT-based fluxes than to their prior fluxes (Fig. A8). As the CAMS prior already agrees reasonably well with TM5-4DVar/GOSAT + IS fluxes, no conclusion on the weights can be drawn here.

The other MIP models, which have lower emission fluxes, show larger mismatches to the OCO-2 XCO_2 measurements for September to November (Fig. A7). Although, for most of these models, assimilating OCO-2 increases the emission fluxes and reduces the difference to the GOSAT-based fluxes (see Figs. A8 and A9), the changes (i.e., the difference between posterior and prior fluxes) are small compared with TM5-4DVar and Baker (see Fig. A8). The larger mismatch to OCO-2 XCO_2 and the smaller posterior–prior flux differences seem to indicate that a smaller weight was given to the OCO-2 measurements compared with the selected MIP models.

In general, the GOSAT flux mismatch and the OCO-2 XCO_2 mismatch is larger in October and November than in September. This is most likely caused by the prior fluxes in September already being closer to the GOSAT-based fluxes than in the other 2 months (see Fig. A9b).

Table A1. Summary of the datasets. The main characteristics and references of the observation and model data are listed. Links to the datasets are provided in the "Data availability" section.

Description	Dataset	Resolution	References
GOSAT XCO_2	GOSAT/RemoTeC v2.4.0	10.5 km footprint	Butz et al. (2011); Butz (2022)
	GOSAT/ACOS v9r(Lite)	10.5 km footprint	Taylor et al. (2022); OCO-2 Science Team et al. (2019)
Validation XCO_2	OCO-2 v11r	1.3 km × 2.3 km footprint	Jacobs et al. (2024); OCO-2/OCO-3 Science Team et al. (2022)
	COCCON Gobabeb	local	Frey et al. (2021); Dubravica et al. (2021)
Model XCO_2 based on in situ data	TM5 − 4DVar/IS	3° × 2°, monthly	Basu et al. (2013)
	CarbonTracker CT2022	3° × 2°, monthly	Peters et al. (2007); Jacobson et al. (2023)
	CAMS v21r1	3.7° × 1.81°, monthly	Chevallier et al. (2005, 2010, 2019); Copernicus Atmosphere Monitoring Service (2020)
In-situ-only inversions	TM5 − 4DVar/IS	3° × 2°, monthly	Basu et al. (2013)
	CarbonTracker CT2022	1° × 1°, monthly	Peters et al. (2007); Jacobson et al. (2023)
	CAMS v20r1	3.7° × 1.81°, monthly	Chevallier et al. (2005, 2010, 2019); Copernicus Atmosphere Monitoring Service (2020)
TM5-4DVar/GOSAT + IS	TM5-4DVar/RemoTeC + IS and TM5-4DVar/ACOS + IS	3° × 2°, monthly	Basu et al. (2013)
TM5-4DVar/OCO-2 + IS	TM5-4DVar of MIP/LNLGIS	1° × 1°, monthly	Basu et al. (2013); Byrne et al. (2023); Baker et al. (2022)
MIP/OCO-2 + IS	MIP/LNLGIS experiment	1° × 1°, monthly	Byrne et al. (2023); Baker et al. (2022)
MIP/IS	MIP/IS experiment		
SIF	GOME-2 Daily_Averaged_SIF	40 km × 40 km/80 km	Joiner et al. (2023)
FLUXCOM	FLUXCOMv1 NEE, RS_V006	0.08° × 0.08°, 8 d	Tramontana et al. (2016); Jung et al. (2020)
GFED	GFED v4.1s	0.25° × 0.25°, monthly	van der Werf et al. (2017, 2015)
$TRENDY_{selection}$	ORCHIDEE S3	0.5° × 0.5°*	Krinner et al. (2005)
	ORCHIDEEv3 S3	2° × 2°*	Vuichard et al. (2019)
	CABLE-POP S3	1° × 1°*	Haverd et al. (2018)
$TRENDY_{others}$	YIBs S3	1° × 1°*	Yue and Unger (2015)
	OCN S3	1° × 1°*	Zaehle et al. (2010)
	ORCHIDEE-CNP S3	2° × 2°*	Goll et al. (2018)
	JSBACH S3	1.86° × 1.88°*	Reick et al. (2021)
	CLASSIC S3	2.80° × 2.81°*	Melton et al. (2020)
	LPJ S3	0.5° × 0.5°*	Poulter et al. (2011)
	CLM5.0 S3	0.94° × 1.25°*	Lawrence et al. (2019)
	DLEM S3	0.5° × 0.5°*	Tian et al. (2015)
	IBIS S3	1° × 1°*	Yuan et al. (2014)
	ISAM S3	0.5° × 0.5°*	Meiyappan et al. (2015)
	ISBA-CTRIP S3	1° × 1°*	Delire et al. (2020)
	JULES-ES-1.0 S3	1.25° × 1.88°*	Sellar et al. (2019)
	LPX-Bern S3	0.5° × 0.5°*	Lienert and Joos (2018)
	SDGVM S3	1° × 1°*	Walker et al. (2017)
	VISIT S3	0.5° × 0.5°*	Kato et al. (2013)
ERA5 meteorological data	ERA5-Land data total precipitation, upper-layer soil moisture, temperature	1° × 1°, monthly	Muñoz Sabater (2019)
MODIS	MODIS (MCD12C1) data	0.05° × 0.05°, 2015	Friedl and Sulla-Menashe (2022)

* All TRENDY model data are provided at a monthly temporal resolution.

Table A2. Monthly fluxes of TM5-4DVar/GOSAT + IS in southern Africa. The monthly fluxes of TM5-4DVar/RemoTeC + IS ("RT + IS"), TM5-4DVar/ACOS + IS (ACOS + IS), and the mean of both are given in teragrams of carbon per month for the whole study region.

Year	Month	RT + IS	ACOS + IS	Mean	Year	Month	RT + IS	ACOS + IS	Mean
2009	4	−157.56	−195.50	−176.53	2014	3	−218.74	−194.84	−206.79
2009	5	−83.13	−102.61	−92.87	2014	4	−160.54	−153.89	−157.21
2009	6	6.71	6.29	6.50	2014	5	−84.72	−81.25	−82.99
2009	7	93.92	109.99	101.96	2014	6	30.42	42.46	36.44
2009	8	163.05	163.17	163.11	2014	7	82.04	99.66	90.85
2009	9	219.63	198.25	208.94	2014	8	95.93	122.13	109.03
2009	10	232.99	144.91	188.95	2014	9	215.17	154.74	184.96
2009	11	140.76	88.81	114.79	2014	10	229.27	176.57	202.92
2009	12	−32.79	−44.05	−38.42	2014	11	199.23	168.02	183.62
2010	1	−144.40	−113.34	−128.87	2014	12	36.93	−35.25	0.84
2010	2	−153.14	−157.85	−155.50	2015	1	−73.64	−86.37	−80.01
2010	3	−144.99	−172.86	−158.93	2015	2	−139.19	−135.31	−137.25
2010	4	−74.81	−121.29	−98.05	2015	3	−153.79	−149.43	−151.61
2010	5	−57.83	−84.45	−71.14	2015	4	−144.28	−131.81	−138.04
2010	6	24.59	16.57	20.58	2015	5	−62.78	−63.61	−63.19
2010	7	69.44	86.01	77.73	2015	6	2.16	22.31	12.24
2010	8	129.28	152.92	141.10	2015	7	49.88	85.39	67.64
2010	9	208.69	202.44	205.57	2015	8	117.11	107.91	112.51
2010	10	239.32	194.63	216.98	2015	9	189.95	139.90	164.93
2010	11	262.58	166.15	214.37	2015	10	225.03	150.79	187.91
2010	12	57.84	−24.29	16.78	2015	11	259.19	212.22	235.70
2011	1	−189.14	−146.26	−167.70	2015	12	112.16	78.85	95.50
2011	2	−229.46	−193.03	−211.24	2016	1	−72.92	−69.47	−71.20
2011	3	−156.96	−183.26	−170.11	2016	2	−148.67	−155.69	−152.18
2011	4	−111.27	−115.31	−113.29	2016	3	−176.60	−134.03	−155.32
2011	5	−70.44	−72.17	−71.31	2016	4	−159.32	−128.91	−144.11
2011	6	22.49	39.77	31.13	2016	5	−77.83	−56.86	−67.35
2011	7	88.88	101.56	95.22	2016	6	28.77	72.38	50.58
2011	8	170.18	183.09	176.63	2016	7	61.68	117.42	89.55
2011	9	214.57	202.08	208.32	2016	8	111.76	166.74	139.25
2011	10	215.25	137.67	176.46	2016	9	178.65	176.21	177.43
2011	11	108.61	83.75	96.18	2016	10	278.49	178.25	228.37
2011	12	−69.23	−42.93	−56.08	2016	11	344.93	213.55	279.24
2012	1	−198.76	−174.22	−186.49	2016	12	126.39	48.90	87.64
2012	2	−204.51	−185.68	−195.09	2017	1	−141.60	−144.98	−143.29
2012	3	−201.66	−209.21	−205.43	2017	2	−218.16	−157.23	−187.70
2012	4	−157.34	−149.79	−153.56	2017	3	−266.37	−195.15	−230.76
2012	5	−85.64	−61.66	−73.65	2017	4	−171.98	−145.48	−158.73
2012	6	26.99	55.95	41.47	2017	5	−87.55	−94.62	−91.09
2012	7	81.80	111.87	96.84	2017	6	−4.45	17.30	6.43
2012	8	105.47	131.05	118.26	2017	7	36.00	108.33	72.17
2012	9	182.86	156.69	169.77	2017	8	125.62	175.62	150.62
2012	10	216.78	172.23	194.51	2017	9	191.89	212.30	202.10
2012	11	130.49	155.95	143.22	2017	10	285.32	197.40	241.36
2012	12	−29.84	−24.57	−27.20	2017	11	233.14	175.95	204.54
2013	1	−195.13	−142.42	−168.78	2017	12	3.21	3.05	3.13
2013	2	−181.41	−141.65	−161.53	2018	1	−131.45	−111.65	−121.55
2013	3	−150.87	−134.34	−142.60	2018	2	−119.89	−127.09	−123.49
2013	4	−133.19	−113.00	−123.10	2018	3	−167.60	−135.00	−151.30
2013	5	−72.44	−40.57	−56.51	2018	4	−208.14	−153.04	−180.59
2013	6	34.37	52.38	43.38	2018	5	−137.36	−102.90	−120.13
2013	7	64.78	85.80	75.29	2018	6	−21.20	23.47	1.14
2013	8	96.91	130.53	113.72	2018	7	29.86	98.30	64.08
2013	9	176.64	185.33	180.99	2018	8	110.99	163.25	137.12
2013	10	219.32	178.29	198.80	2018	9	202.02	201.28	201.65
2013	11	249.06	191.11	220.08	2018	10	182.51	179.17	180.84
2013	12	202.08	64.14	133.11	2018	11	223.74	184.91	204.33
2014	1	−79.09	−119.87	−99.48	2018	12	226.30	148.33	187.31
2014	2	−187.16	−169.20	−178.18					

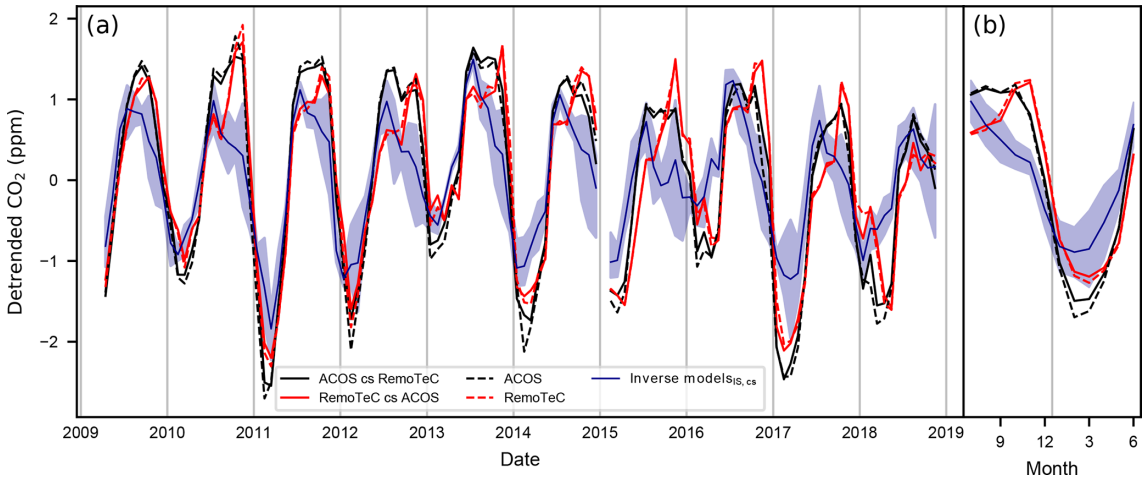

Figure A1. Monthly southern African detrended CO_2 concentrations measured by GOSAT. GOSAT/ACOS is given in black, while GOSAT/RemoTeC is given in red. Dashed lines show the mean CO_2 concentrations over the whole dataset. The mean CO_2 concentrations of the soundings included in both datasets, ACOS and RemoTeC, are given as solid lines. "cs" stands for co-sampled and indicates that only soundings also included in the other dataset are considered. The deviations due to different sampling are on a sub-part-per-million scale and do not explain the differences between ACOS and RemoTeC. Modeled posterior CO_2 concentrations of the in-situ-only inversions are co-sampled (cs) on GOSAT and depicted as the mean (in blue) for comparison. The shading indicates the range among the individual in-situ-only inversions. Panel **(b)** shows the mean seasonal cycle for 2009–2018, with the standard deviation over the years given as shading.

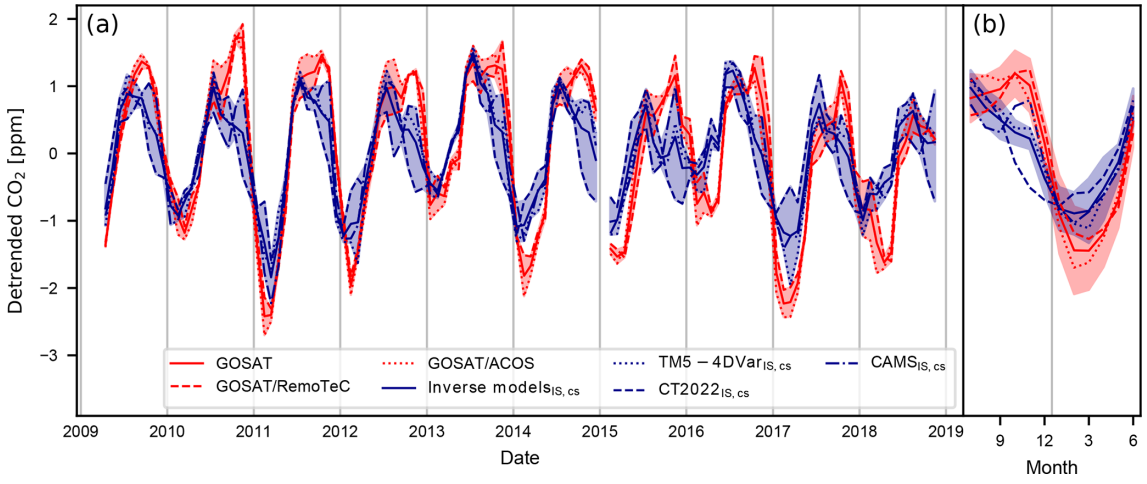

Figure A2. Monthly southern African detrended CO_2 concentrations given by inversions and satellites. Like Fig. 1 but with detrended XCO_2 of individual in-situ-only inversions co-sampled (cs) on the GOSAT measurements in dark blue (CT2022 – dashed; CAMS – dot-dash; and TM5-4DVar/IS – dotted). Panel **(a)** gives the monthly mean CO_2 concentrations, whereas panel **(b)** shows the mean seasonal cycle for 2009–2018. The shading indicates the range among GOSAT/ACOS and GOSAT/RemoTeC and the range among the three in-situ-only inversions in panel **(a)**. In panel **(b)**, the shading indicates the standard deviation over the year.

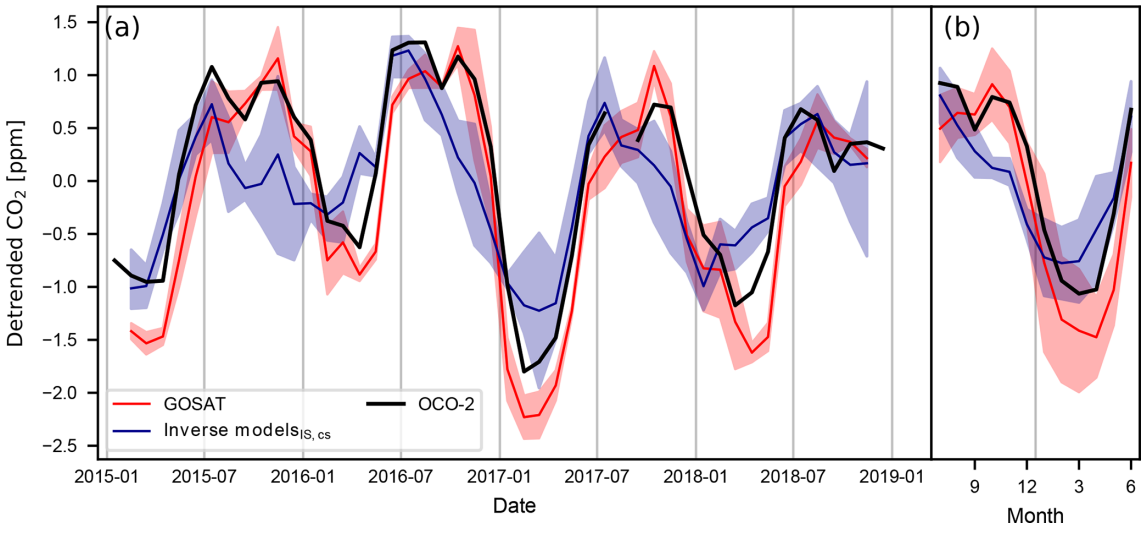

Figure A3. Monthly southern African detrended CO_2 concentrations given by inversions and satellites. Like Fig. 1 but with detrended XCO_2 measurements of OCO-2 (in black) for the time period from 2015 to 2018. Panel **(a)** gives the monthly mean CO_2 concentrations, whereas panel **(b)** shows the mean seasonal cycle for 2015–2018. The shading indicates the range among GOSAT/ACOS and GOSAT/RemoTeC and the range among the three in-situ-only inversions in panel **(a)**. In panel **(b)**, the shading indicates the standard deviation over the years.

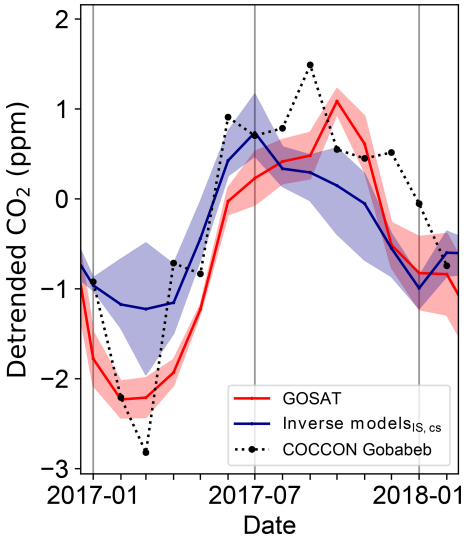

Figure A4. Monthly southern African detrended CO_2 concentrations given by inversions, satellites, and COCCON measurements. Like Fig. 1 but only for January 2017–February 2018 and with detrended XCO_2 measurements from the Gobabeb COCCON station (in black). The full dataset of COCCON measurements is used, without performing a co-sampling on GOSAT measurements or further filtering.

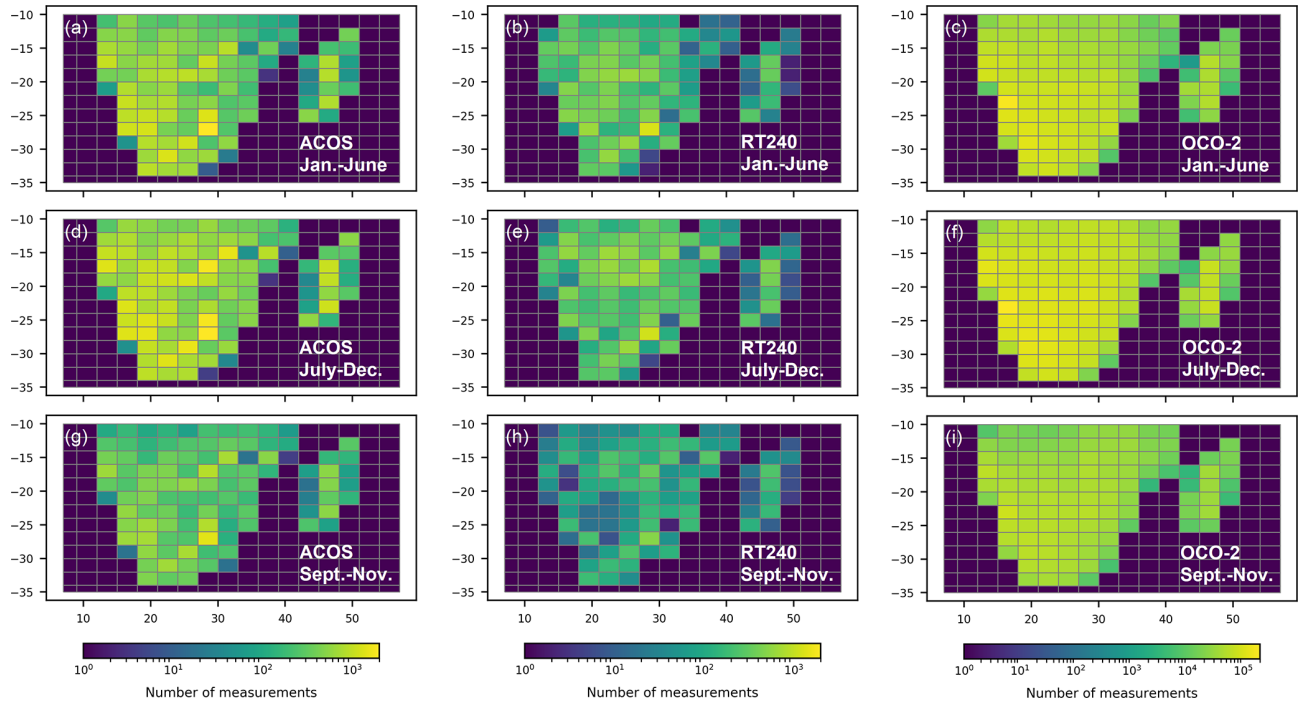

Figure A5. Number and distribution of satellite CO_2 concentration measurements above southern Africa. **(a, d, g)** Total number of GOSAT/ACOS, **(b, e, h)** GOSAT/RemoTeC, and **(c, f, i)** OCO-2 data per $3° \times 2°$ grid cell for **(a–c)** the months of carbon uptake (January–June), **(d–f)** the emission season (July–December), and **(g–i)** the month with the strongest emissions. GOSAT/ACOS and GOSAT/RemoTeC measurements from 2009 to 2018 and OCO-2 measurements from September 2014 to 2018 are included. The maximum of the color scale is the same for all time periods but different for OCO-2 compared with GOSAT/ACOS and GOSAT/RemoTeC. Compared with GOSAT/ACOS, GOSAT/RemoTeC has a reduced number of measurements, as the RemoTeC algorithm applies stricter filtering of the GOSAT soundings.

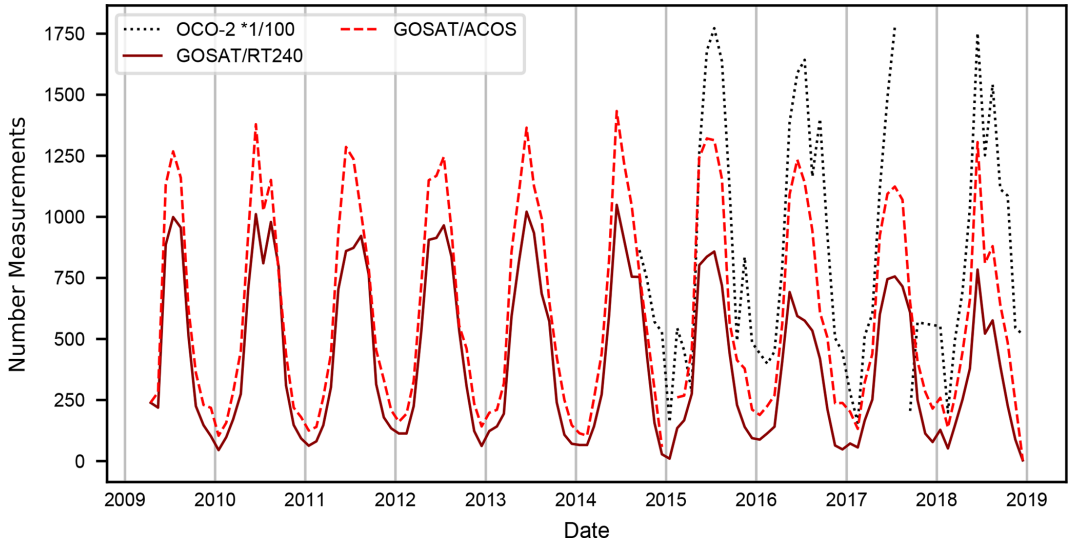

Figure A6. Number of satellite measurements per month. The numbers of satellite measurements in the GOSAT/ACOS (dashed red line), GOSAT/RemoTeC (solid dark-red line), and OCO-2 (dotted gray line) datasets are given. Note that the number of OCO-2 measurements is shown divided by 100 to enable a comparison to the much less abundant GOSAT measurements.

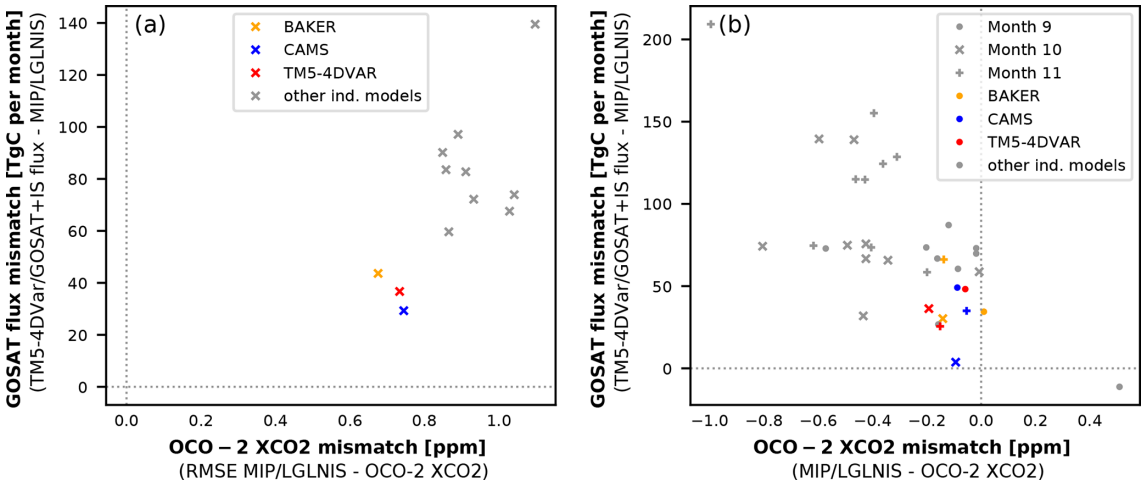

Figure A7. Mismatch between GOSAT-informed and OCO-2-informed fluxes versus the mismatch between OCO-2-informed simulated XCO_2 and OCO-2-measured XCO_2. For the MIP/OCO-2 + IS inversions, 5 % of the OCO-2 measurements are withheld for validation purposes and modeled XCO_2 values co-sampled on the measurements are provided for each model except CSU. Panel **(a)** gives the RMSE of the OCO-2 measurements and the modeled co-sampled XCO_2 from September to November for each model. In panel **(b)**, the mean differences in the OCO-2 measurements and modeled co-samples for each month and model are given. In both panels, the OCO-2 XCO_2 mismatch is plotted against the difference in the monthly TM5-4DVar/GOSAT + IS and individual MIP/OCO-2 + IS CO_2 fluxes for the strongest emission period from September to November. The MIP models Baker, CAMS, and TM5-4DVar are highlighted in yellow, blue, and red, respectively. The other individual MIP models are given in gray. The three highlighted models show the smallest OCO-2 XCO_2 mismatch and the smallest difference from the monthly fluxes of TM5-4DVar/GOSAT + IS (with the exception of Baker in September; **b**).

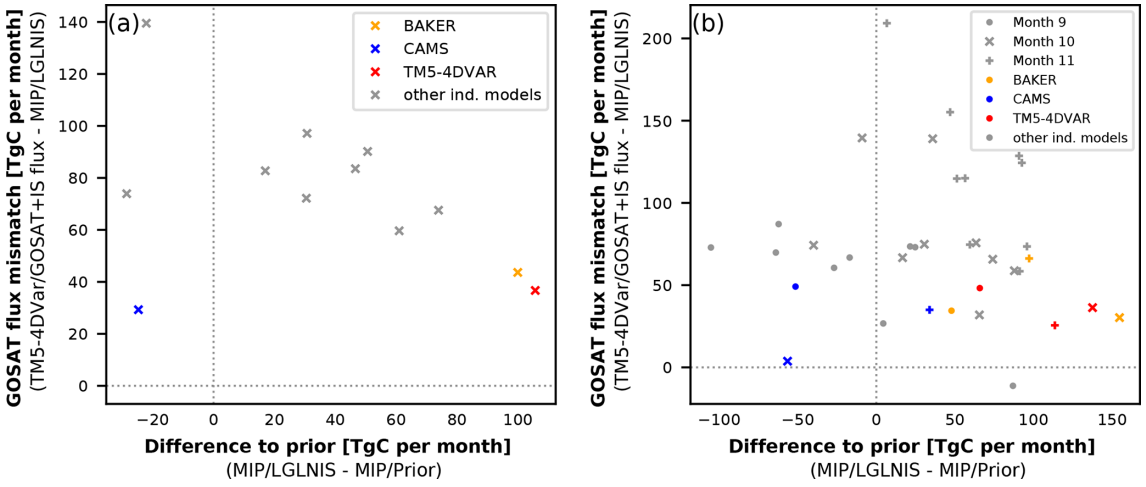

Figure A8. Mismatch between GOSAT-informed and OCO-2-informed fluxes versus the difference between OCO-2-informed fluxes and model prior fluxes. The individual MIP models differ with respect to their assumed prior fluxes. In this figure, the differences in the monthly posterior to the prior fluxes (x axis) and to the GOSAT-based fluxes (TM5-4DVar/GOSAT + IS, y axis) are compared. Differences are calculated using the monthly flux over the whole study region and the time period from 2015 to 2018. Panel **(a)** shows the mean over September to November, the time of the strongest CO_2 emissions. In panel **(b)**, the differences are given for each of the three individual months. The MIP models Baker, CAMS, and TM5-4DVar are highlighted in yellow, blue, and red, respectively. The other individual MIP models are given in gray. For most of the models, the assimilation of OCO-2 measurements increases the mean monthly fluxes from September to November (difference from prior larger than zero). Only for CAMS, UT, and some models in September are the mean posterior fluxes smaller than the prior fluxes.

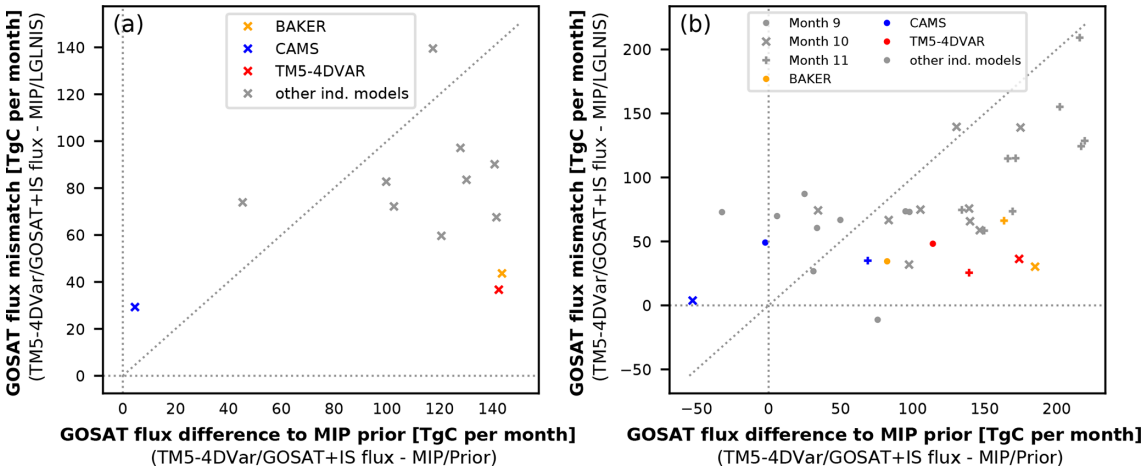

Figure A9. Mismatch between GOSAT-informed and OCO-2-informed fluxes versus the difference between GOSAT-informed fluxes and OCO-2 MIP prior fluxes. The differences in the monthly GOSAT inversion fluxes (TM5-4DVar/GOSAT + IS) compared with the MIP posterior (y axis) and MIP prior fluxes (x axis) for the individual MIP models are given. Panel **(a)** gives the mean differences for the months from September to November. Panel **(b)** shows the differences for the individual months. The MIP models Baker, CAMS, and TM5-4DVar are highlighted in yellow, blue, and red, respectively. The other individual MIP models are given in gray. The 1 : 1 line is given as a dotted gray line. For most of the MIP models, assimilating OCO-2 reduces the flux difference to the GOSAT-based fluxes (i.e., markers are below the 1 : 1 line).

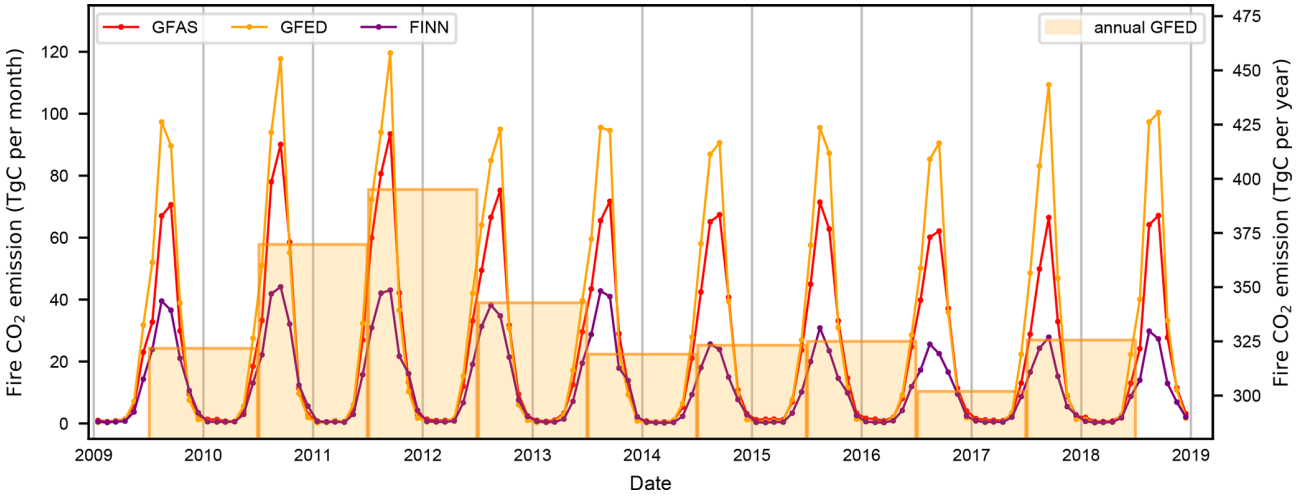

Figure A10. The CO_2 fire emissions in southern Africa. The monthly CO_2 fire emissions collected by three fire emission databases: GFED (in orange), the Global Fire Assimilation System (GFAS; Kaiser et al., 2012; Copernicus Atmosphere Monitoring Service, 2022; in red), and the Fire INventory from NCAR (FINN; Wiedinmyer et al., 2011, 2021; in purple). Furthermore, the annual (July–June) GFED fire emissions are shown on the right-hand y axis. Please note that the right-hand y axis starts at 280 TgC yr^{-1} for better visualization of the fire emissions.

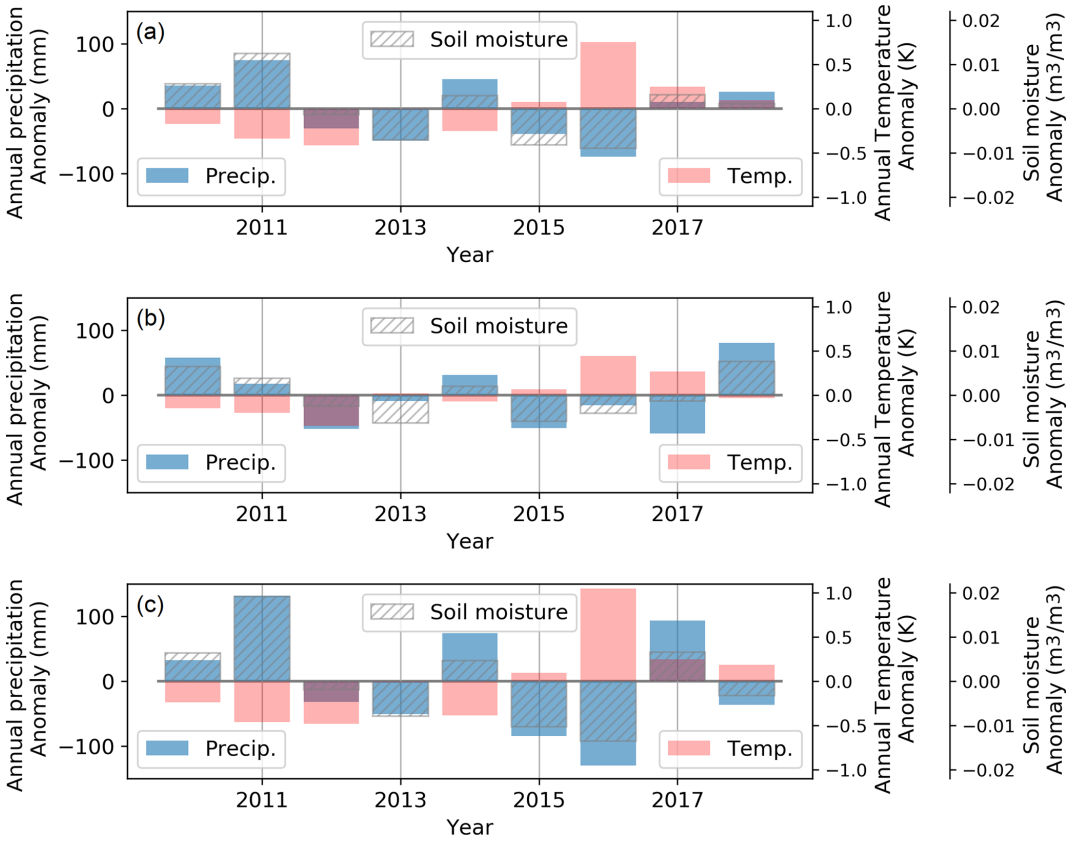

Figure A11. Climate anomalies. The annual anomalies of ERA5 precipitation, temperature, and upper-layer soil moisture are displayed using solid blue, solid red, and gray hatching, respectively. The annual anomalies are calculated by subtracting the individual long-term mean of the annual values and are given for the whole study region in panel **(a)**, for the northern subregion in panel **(b)**, and for the southern subregion in panel **(c)**.

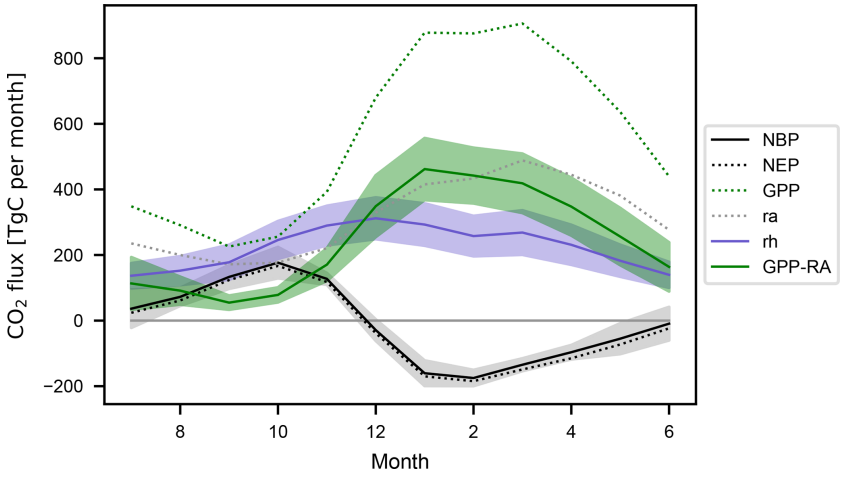

Figure A12. Mean monthly CO_2 net and gross fluxes. Like Fig. 8a but also including the GPP and RA of the TRENDY selection.

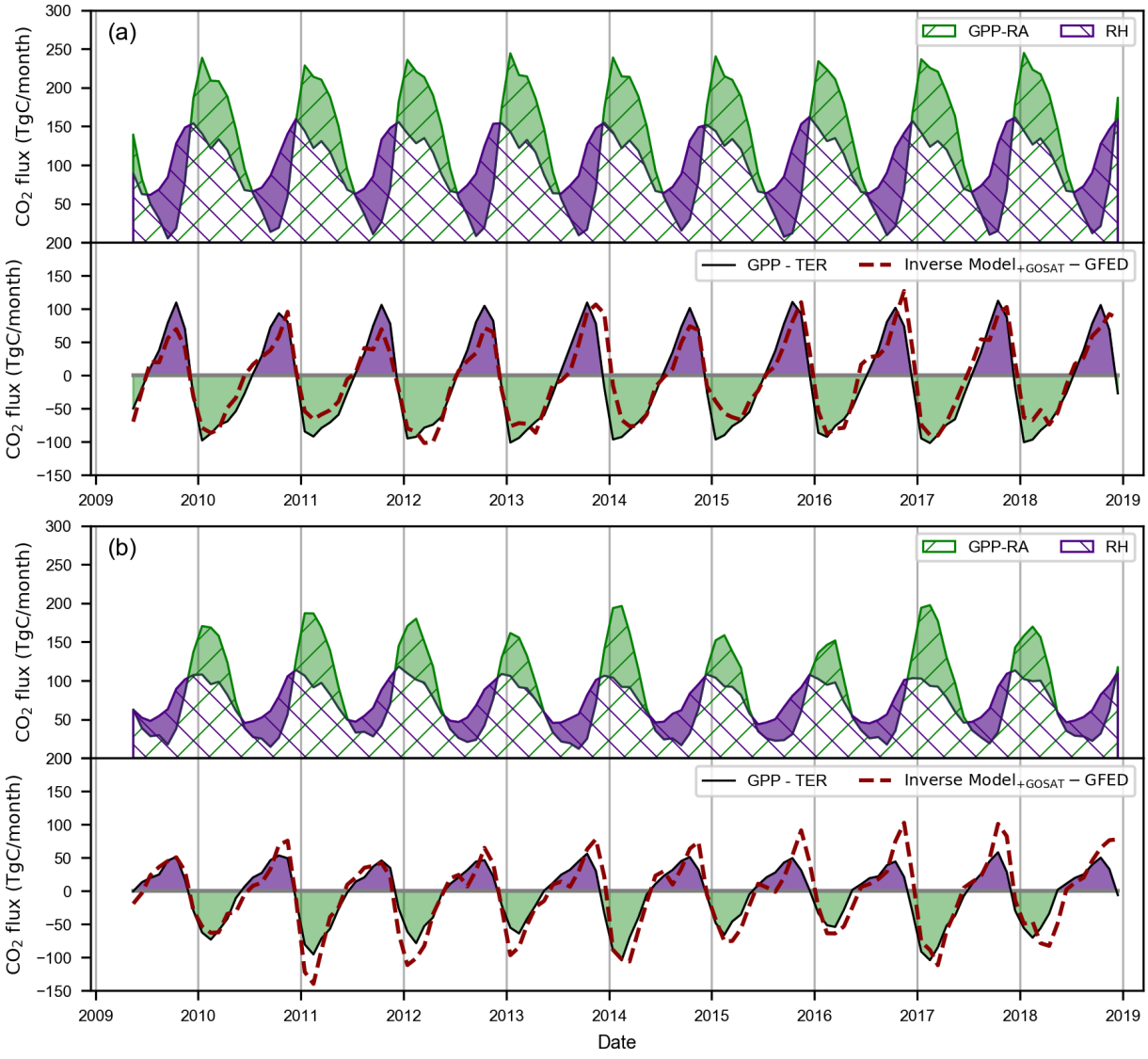

Figure A13. Monthly CO_2 fluxes in the northern **(a)** and southern **(b)** subregions. The monthly NEE, NPP (GPP − RA), and RH fluxes from the selected TRENDY models are given in black, green, and violet, respectively, for the northern southern African region in panel **(a)**. The TM5-4DVar/GOSAT + IS–GFED NEE fluxes are additionally shown as a dotted red line. The same is given in panel **(b)** for the southern subregion.

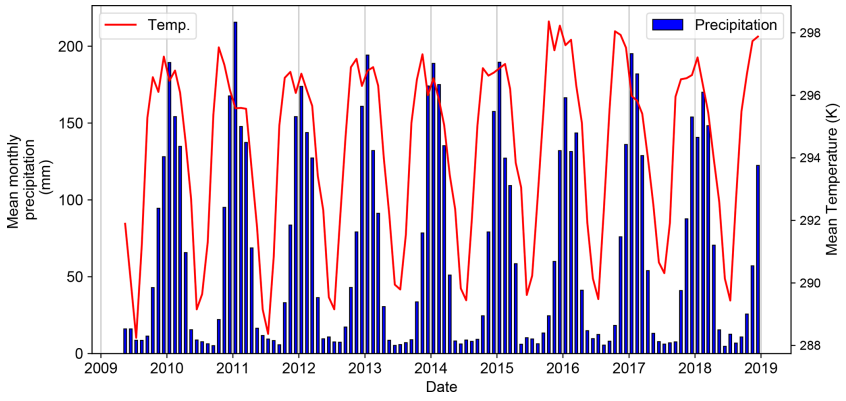

Figure A14. Mean monthly precipitation and mean temperature over southern Africa. The mean monthly precipitation is given as blue bars, whereas the mean temperature is shown using a solid red line.

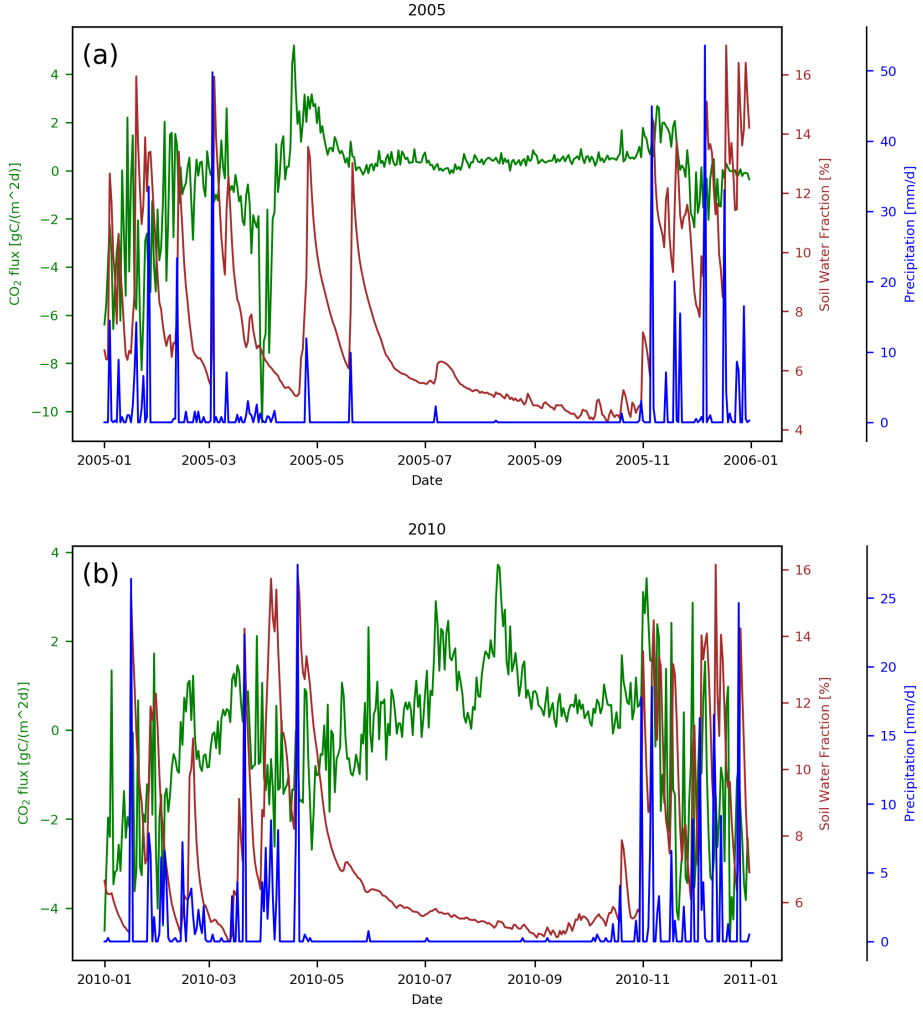

Figure A15. Local data from the FLUXNET eddy-covariance flux tower in Kruger National Park. Daily mean net carbon fluxes (green), precipitation (blue), and soil moisture (red) measured by the ZA-Kru FLUXNET station (Archibald et al., 2009; Scholes, 2013). Panel **(a)** shows the year 2005, whereas panel **(b)** shows 2010.

Code availability. The code used in this study is available from https://doi.org/10.5281/zenodo.12528504 (Metz, 2024) or GitHub (https://github.com/ATMO-IUP-UHEI/MetzEtAl2024, last access: 25 June 2024).

Data availability. GOSAT/RemoTeC2.4.0 XCO_2 data can be obtained from Zenodo: https://doi.org/10.5281/zenodo.5886662 (Butz, 2022). GOSAT/ACOS data are available from https://oco2.gesdisc.eosdis.nasa.gov/data/GOSAT_TANSO_Level2/ACOS_L2_Lite_FP.9r/ (OCO-2 Science Team, 2019, https://doi.org/10.5067/VWSABTO7ZII4). OCO-2 data are available from https://doi.org/10.5067/8E4VLCK16O6Q (OCO-2/OCO-3 Science Team et al., 2022). CarbonTracker CT2022 CO_2 fluxes and concentrations can be downloaded from https://gml.noaa.gov/aftp/products/carbontracker/co2/CT2022/fluxes/monthly/ and https://gml.noaa.gov/aftp/products/carbontracker/co2/CT2022/molefractions/co2_total_monthly/ (Jacobson et al., 2023, https://doi.org/10.25925/z1gj-3254), respectively. CAMS concentrations and fluxes can be found at https://ads.atmosphere.copernicus.eu/cdsapp#!/dataset/cams-global-greenhouse-gas-inversion (Copernicus Atmosphere Monitoring Service, 2020). GFAS emission records are available from https://ads.atmosphere.copernicus.eu/datasets/cams-global-fire-emissions-gfas (Copernicus Atmosphere Monitoring Service, 2022). CAMS and GFAS data were generated using Copernicus Atmosphere Monitoring Service information 2021; neither the European Commission nor the European Centre for Medium-Range Weather Forecasts (ECMWF) is responsible for any use that may be made of the information they contain. The MIP data can be downloaded from https://gml.noaa.gov/ccgg/OCO2_v10mip/ (Baker et al., 2022). GFED fire emissions are available from https://www.geo.vu.nl/~gwerf/GFED/GFED4/ (van der Werf et al., 2015). FINN data were retrieved from the American National Center for Atmospheric Research: https://www.acom.ucar.edu/Data/fire/ (Wiedinmyer et al., 2021). ERA5-Land data records contain modified Copernicus Atmosphere Monitoring Service information 2021 available from the Climate Data Store https://cds.climate.copernicus.eu/cdsapp#!/dataset/reanalysis-era5-land-monthly-means (Muñoz Sabater, 2019, https://doi.org/10.24381/cds.68d2bb30). TRENDYv9 model output is available upon request from https://mdosullivan.github.io/GCB/ (Sitch et al., 2020). FLUXCOM products are available from http://fluxcom.org/CF-Download/ (Jung et al., 2020, https://doi.org/10.5194/bg-17-1343-2020; Tramontana et al., 2016, https://doi.org/10.5194/bg-13-4291-2016). Data from the ZA-Kru FLUXNET station can be downloaded from FLUXNET: https://fluxnet.org/data/fluxnet2015-dataset/ (Scholes, 2013, https://doi.org/10.18140/FLX/1440188). The Gobabeb COCCON station data are available from https://secondary-data-archive.nilu.no/evdc/ftir/coccon/gobabeb/version2/ (Dubravica et al., 2021, https://doi.org/10.48477/coccon.pf10.gobabeb.R02). MODIS MCD12C1 data are available from https://search.earthdata.nasa.gov/search with the following DOI: https://doi.org/10.5067/MODIS/MCD12C1.061 (Friedl and Sulla-Menashe, 2022). "L2 Daily Solar-Induced Fluorescence (SIF) from MetOp-A GOME-2" V2 data are available from https://search.earthdata.nasa.gov/ (Joiner et al., 2023, https://doi.org/10.3334/ORNLDAAC/2292). Monthly TM5-4DVar data are given in Table A2.

Author contributions. SNV, AB, and EMM were involved in the conceptualization process and the development of the methodology. SB performed the dedicated TM5-4DVar runs. EMM conducted the formal analysis and created the figures, under the supervision of AB and SNV. EMM wrote the original draft. All authors contributed to the interpretation of the results and the editing and review of the manuscript.

Competing interests. The contact author has declared that none of the authors has any competing interests.

Disclaimer. Publisher's note: Copernicus Publications remains neutral with regard to jurisdictional claims made in the text, published maps, institutional affiliations, or any other geographical representation in this paper. While Copernicus Publications makes every effort to include appropriate place names, the final responsibility lies with the authors.

Acknowledgements. The authors gratefully acknowledge the SDS@hd data storage service, supported by the Ministry of Science, Research and the Arts Baden-Württemberg (MWK), and the computing resources provided by the Deutsche Klimarechenzentrum (DKRZ; project no. bb1170). Eva-Marie Metz acknowledges a doctoral scholarship from the German Academic Scholarship Foundation. The authors also wish to thank the Japanese Aerospace Exploration Agency, the National Institute for Environmental Studies, and the Ministry of Environment for the GOSAT data and their continuous support as part of a joint research agreement. Moreover, we thank the OCO-2 science team for producing the GOSAT/ACOS L2 XCO_2 data. OCO-2 data were produced by the OCO-2 project at the Jet Propulsion Laboratory, California Institute of Technology, and obtained from the OCO-2 data archive maintained at the NASA Goddard Earth Science Data and Information Services Center. CarbonTracker CT2022 results were provided by NOAA ESRL, Boulder, Colorado, USA: http://carbontracker.noaa.gov (last access: 17 September 2024). Finally, we thank Stephen Sitch, Pierre Friedlingstein, and all modelers of the "Trends and drivers of the regional scale terrestrial sources and sinks of carbon dioxide" (TRENDY) project. The long-term operation of the Gobabeb COCCON site in Namibia is supported by ESA via the COCCON-PROCEEDS series of projects (contract no. 4000121212) and COCCON-OPERA (contract no. 4000140431/23/I-DT-Ir).

Financial support. Funding for the development of RemoTeC was provided by the German Research Foundation (DFG; grant BU2599/1-1); operations and data storage were also supported by the DFG (grant no. INST 35/1503-1 FUGG). Sourish Basu was supported by NASA (grant no. 80NSSC20K0818).

Review statement. This paper was edited by Kerneels Jaars and reviewed by Thomas E. Taylor and one anonymous referee.

References

Ahlström, A., Raupach, M. R., Schurgers, G., Smith, B., Arneth, A., Jung, M., Reichstein, M., Canadell, J. G., Friedlingstein, P., Jain, A. K., Kato, E., Poulter, B., Sitch, S., Stocker, B. D., Viovy, N., Wang, Y. P., Wiltshire, A., Zaehle, S., and Zeng, N.: The dominant role of semi-arid ecosystems in the trend and variability of the land CO_2 sink, Science, 348, 895–899, https://doi.org/10.1126/science.aaa1668, 2015.

Archibald, S. A., Kirton, A., van der Merwe, M. R., Scholes, R. J., Williams, C. A., and Hanan, N.: Drivers of inter-annual variability in Net Ecosystem Exchange in a semi-arid savanna ecosystem, South Africa, Biogeosciences, 6, 251–266, https://doi.org/10.5194/bg-6-251-2009, 2009.

Baker, D. F., Basu, S., Bertolacci, M., Chevallier, F., Cressie, N., Crowell, S., Deng, F., He, W., Jacobson, A. R., Janardanan, R., Jiang, F., Johnson, M. S., Jones, D. B. A., Liu, J., Liu, Z., Maksyutov, S., Miller, S. M., Philip, S., Schuh, A., Weir, B., Zammit-Mangion, A., and Zeng, N.: v10 Orbiting Carbon Observatory-2 model intercomparison project, NOAA Global Monitoring Laboratory [data set], https://gml.noaa.gov/ccgg/OCO2_v10mip/ (last access: 6 May 2022), 2022.

Bastos, A., O'Sullivan, M., Ciais, P., Makowski, D., Sitch, S., Friedlingstein, P., Chevallier, F., Rödenbeck, C., Pongratz, J., Luijkx, I. T., Patra, P. K., Peylin, P., Canadell, J. G., Lauerwald, R., Li, W., Smith, N. E., Peters, W., Goll, D. S., Jain, A. K., Kato, E., Lienert, S., Lombardozzi, D. L., Haverd, V., Nabel, J. E. M. S., Poulter, B., Tian, H., Walker, A. P., and Zaehle, S.: Sources of Uncertainty in Regional and Global Terrestrial CO_2 Exchange Estimates, Global Biogeochem. Cy., 34, e2019GB006393, https://doi.org/10.1029/2019GB006393, 2020.

Basu, S., Guerlet, S., Butz, A., Houweling, S., Hasekamp, O., Aben, I., Krummel, P., Steele, P., Langenfelds, R., Torn, M., Biraud, S., Stephens, B., Andrews, A., and Worthy, D.: Global CO2 fluxes estimated from GOSAT retrievals of total column CO2, Atmos. Chem. Phys., 13, 8695–8717, https://doi.org/10.5194/acp-13-8695-2013, 2013.

Birch, H. F.: Mineralisation of plant nitrogen following alternate wet and dry conditions, Plant Soil, 20, 43–49, https://doi.org/10.1007/bf01378096, 1964.

Buchwitz, M., Reuter, M., Schneising, O., Hewson, W., Detmers, R. G., Boesch, H., Hasekamp, O. P., Aben, I., Bovensmann, H., Burrows, J. P., Butz, A., Chevallier, F., Dils, B., Frankenberg, C., Heymann, J., Lichtenberg, G., Mazière, M. de, Notholt, J., Parker, R., Warneke, T., Zehner, C., Griffith, D., Deutscher, N. M., Kuze, A., Suto, H., and Wunch, D.: Global satellite observations of column-averaged carbon dioxide and methane: The GHG-CCI XCO_2 and XCH4 CRDP3 data set, Remote Sens. Environ., 203, 276–295, https://doi.org/10.1016/j.rse.2016.12.027, 2017.

Butz, A.: RemoTeC full-physics retrieval GOSAT/TANSO-FTS Level 2 bias-corrected XCO_2 version 2.4.0 operated at Heidelberg University, Zenodo [data set], https://doi.org/10.5281/zenodo.5886662, 2022.

Butz, A., Guerlet, S., Hasekamp, O., Schepers, D., Galli, A., Aben, I., Frankenberg, C., Hartmann, J.-M., Tran, H., Kuze, A., Keppel-Aleks, G., Toon, G., Wunch, D., Wennberg, P., Deutscher, N., Griffith, D., Macatangay, R., Messerschmidt, J., Notholt, J., and Warneke, T.: Toward accurate CO_2 and CH_4 observations from GOSAT, Geophys. Res. Lett., 38, L14812, https://doi.org/10.1029/2011GL047888, 2011.

Byrne, B., Baker, D. F., Basu, S., Bertolacci, M., Bowman, K. W., Carroll, D., Chatterjee, A., Chevallier, F., Ciais, P., Cressie, N., Crisp, D., Crowell, S., Deng, F., Deng, Z., Deutscher, N. M., Dubey, M. K., Feng, S., García, O. E., Griffith, D. W. T., Herkommer, B., Hu, L., Jacobson, A. R., Janardanan, R., Jeong, S., Johnson, M. S., Jones, D. B. A., Kivi, R., Liu, J., Liu, Z., Maksyutov, S., Miller, J. B., Miller, S. M., Morino, I., Notholt, J., Oda, T., O'Dell, C. W., Oh, Y.-S., Ohyama, H., Patra, P. K., Peiro, H., Petri, C., Philip, S., Pollard, D. F., Poulter, B., Remaud, M., Schuh, A., Sha, M. K., Shiomi, K., Strong, K., Sweeney, C., Té, Y., Tian, H., Velazco, V. A., Vrekoussis, M., Warneke, T., Worden, J. R., Wunch, D., Yao, Y., Yun, J., Zammit-Mangion, A., and Zeng, N.: National CO_2 budgets (2015–2020) inferred from atmospheric CO_2 observations in support of the global stocktake, Earth Syst. Sci. Data, 15, 963–1004, https://doi.org/10.5194/essd-15-963-2023, 2023.

Chevallier, F., Engelen, R. J., and Peylin, P.: The contribution of AIRS data to the estimation of CO_2 sources and sinks, Geophys. Res. Lett., 32, L23801, https://doi.org/10.1029/2005GL024229, 2005.

Chevallier, F., Ciais, P., Conway, T. J., Aalto, T., Anderson, B. E., Bousquet, P., Brunke, E. G., Ciattaglia, L., Esaki, Y., and Fröhlich, M.: CO_2 surface fluxes at grid point scale estimated from a global 21 year reanalysis of atmospheric measurements, J. Geophys. Res.-Atmos., 115, D21307, https://doi.org/10.1029/2010JD013887, 2010.

Chevallier, F., Remaud, M., O'Dell, C. W., Baker, D., Peylin, P., and Cozic, A.: Objective evaluation of surface- and satellite-driven carbon dioxide atmospheric inversions, Atmos. Chem. Phys., 19, 14233–14251, https://doi.org/10.5194/acp-19-14233-2019, 2019.

Ciais, P., Piao, S.-L., Cadule, P., Friedlingstein, P., and Chédin, A.: Variability and recent trends in the African terrestrial carbon balance, Biogeosciences, 6, 1935–1948, https://doi.org/10.5194/bg-6-1935-2009, 2009.

Copernicus Atmosphere Monitoring Service: CAMS global inversion-optimised greenhouse gas fluxes and concentrations, Copernicus Atmosphere Monitoring Service (CAMS) Atmosphere Data Store [data set], https://ads.atmosphere.copernicus.eu/cdsapp#!/dataset/cams-global-greenhouse-gas-inversion (last access: 7 October 2021), 2020.

Copernicus Atmosphere Monitoring Service: CAMS global biomass burning emissions based on fire radiative power (GFAS), Copernicus Atmosphere Monitoring Service (CAMS) Atmosphere Data Store [data set], https://ads.atmosphere.copernicus.eu/datasets/cams-global-fire-emissions-gfas (last access: 2 February 2024), 2022.

Delire, C., Séférian, R., Decharme, B., Alkama, R., Calvet, J.-C., Carrer, D., Gibelin, A.-L., Joetzjer, E., Morel, X., Rocher, M., and Tzanos, D.: The Global Land Carbon Cycle Simulated With ISBA-CTRIP: Improvements Over the

Last Decade, J. Adv. Model. Earth Sy., 12, e2019MS001886, https://doi.org/10.1029/2019MS001886, 2020.

Detmers, R. G., Hasekamp, O., Aben, I., Houweling, S., Leeuwen, T. T., Butz, A., Landgraf, J., Köhler, P., Guanter, L., and Poulter, B.: Anomalous carbon uptake in Australia as seen by GOSAT, Geophys. Res. Lett., 42, 8177–8184, https://doi.org/10.1002/2015GL065161, 2015.

Dubravica, D., Hase, F., Alberti, C., Frey, M., and Marais, E.: COCCON Version 2 dataset from atmospheric observatory of Gobabeb (Namibia) available at the EVDC Data Handling Facilities covering start date Jan 9th 2017 to end date Nov 27th 2020, COCCON – Central Facility/EVDC – ESA Atmospheric Validation Data Centre [data set], https://doi.org/10.48477/coccon.pf10.gobabeb.R02, 2021 (data available at: https://secondary-data-archive.nilu.no/evdc/ftir/coccon/gobabeb/version2/, last access: 27 March 2023).

Edwards, D. P., Emmons, L. K., Gille, J. C., Chu, A., Attié, J.-L., Giglio, L., Wood, S. W., Haywood, J., Deeter, M. N., Massie, S. T., Ziskin, D. C., and Drummond, J. R.: Satellite-observed pollution from Southern Hemisphere biomass burning, J. Geophys. Res., 111, D14312, https://doi.org/10.1029/2005JD006655, 2006.

Ernst, Y., Archibald, S., Balzter, H., Chevallier, F., Ciais, P., Fischer, C. G., Gaubert, B., Higginbottom, T., Higgins, S., Lawal, S., Lacroix, F., Lauerwald, R., Lourenco, M., Martens, C., Mengistu, A. G., Merbold, L., Mitchard, E., Moyo, M., Nguyen, H., O'sullivan, M., Rodríguez-Veiga, P., Rosan, T., Rosentreter, J., Ryan, C., Scheiter, S., Sitch, S., Stevens, N., Tagesson, T., Tian, H., Wang, M., Woon, J. S., Zheng, B., Zhou, Y., and Scholes, R. J.: The African Regional Greenhouse Gases Budget (2010–2019), Global Biogeochem. Cy., 38, e2023GB008016, https://doi.org/10.1029/2023GB008016, 2024.

Fan, Z., Neff, J. C., and Hanan, N. P.: Modeling pulsed soil respiration in an African savanna ecosystem, Agr. Forest Meteorol., 200, 282–292, https://doi.org/10.1016/j.agrformet.2014.10.009, 2015.

Foster, K. T., Sun, W., Shiga, Y. P., Mao, J., and Michalak, A. M.: Multiscale assessment of North American terrestrial carbon balance, Biogeosciences, 21, 869–891, https://doi.org/10.5194/bg-21-869-2024, 2024.

Frey, M., Sha, M. K., Hase, F., Kiel, M., Blumenstock, T., Harig, R., Surawicz, G., Deutscher, N. M., Shiomi, K., Franklin, J. E., Bösch, H., Chen, J., Grutter, M., Ohyama, H., Sun, Y., Butz, A., Mengistu Tsidu, G., Ene, D., Wunch, D., Cao, Z., Garcia, O., Ramonet, M., Vogel, F., and Orphal, J.: Building the COllaborative Carbon Column Observing Network (COCCON): long-term stability and ensemble performance of the EM27/SUN Fourier transform spectrometer, Atmos. Meas. Tech., 12, 1513–1530, https://doi.org/10.5194/amt-12-1513-2019, 2019.

Frey, M. M., Hase, F., Blumenstock, T., Dubravica, D., Groß, J., Göttsche, F., Handjaba, M., Amadhila, P., Mushi, R., Morino, I., Shiomi, K., Sha, M. K., de Mazière, M., and Pollard, D. F.: Long-term column-averaged greenhouse gas observations using a COCCON spectrometer at the high-surface-albedo site in Gobabeb, Namibia, Atmos. Meas. Tech., 14, 5887–5911, https://doi.org/10.5194/amt-14-5887-2021, 2021.

Friedl, M. and Sulla-Menashe, D.: MODIS/Terra+Aqua Land Cover Type Yearly L3 Global 0.05Deg CMG V061, NASA EOSDIS Land Processes Distributed Active Archive Center [data set], https://doi.org/10.5067/MODIS/MCD12C1.061, 2022 (data available at: https://search.earthdata.nasa.gov/search, last access: 24 March 2024).

Friedlingstein, P., O'Sullivan, M., Jones, M. W., Andrew, R. M., Hauck, J., Olsen, A., Peters, G. P., Peters, W., Pongratz, J., Sitch, S., Le Quéré, C., Canadell, J. G., Ciais, P., Jackson, R. B., Alin, S., Aragão, L. E. O. C., Arneth, A., Arora, V., Bates, N. R., Becker, M., Benoit-Cattin, A., Bittig, H. C., Bopp, L., Bultan, S., Chandra, N., Chevallier, F., Chini, L. P., Evans, W., Florentie, L., Forster, P. M., Gasser, T., Gehlen, M., Gilfillan, D., Gkritzalis, T., Gregor, L., Gruber, N., Harris, I., Hartung, K., Haverd, V., Houghton, R. A., Ilyina, T., Jain, A. K., Joetzjer, E., Kadono, K., Kato, E., Kitidis, V., Korsbakken, J. I., Landschützer, P., Lefèvre, N., Lenton, A., Lienert, S., Liu, Z., Lombardozzi, D., Marland, G., Metzl, N., Munro, D. R., Nabel, J. E. M. S., Nakaoka, S.-I., Niwa, Y., O'Brien, K., Ono, T., Palmer, P. I., Pierrot, D., Poulter, B., Resplandy, L., Robertson, E., Rödenbeck, C., Schwinger, J., Séférian, R., Skjelvan, I., Smith, A. J. P., Sutton, A. J., Tanhua, T., Tans, P. P., Tian, H., Tilbrook, B., van der Werf, G., Vuichard, N., Walker, A. P., Wanninkhof, R., Watson, A. J., Willis, D., Wiltshire, A. J., Yuan, W., Yue, X., and Zaehle, S.: Global Carbon Budget 2020, Earth Syst. Sci. Data, 12, 3269–3340, https://doi.org/10.5194/essd-12-3269-2020, 2020.

Friedlingstein, P., O'Sullivan, M., Jones, M. W., Andrew, R. M., Bakker, D. C. E., Hauck, J., Landschützer, P., Le Quéré, C., Luijkx, I. T., Peters, G. P., Peters, W., Pongratz, J., Schwingshackl, C., Sitch, S., Canadell, J. G., Ciais, P., Jackson, R. B., Alin, S. R., Anthoni, P., Barbero, L., Bates, N. R., Becker, M., Bellouin, N., Decharme, B., Bopp, L., Brasika, I. B. M., Cadule, P., Chamberlain, M. A., Chandra, N., Chau, T.-T.-T., Chevallier, F., Chini, L. P., Cronin, M., Dou, X., Enyo, K., Evans, W., Falk, S., Feely, R. A., Feng, L., Ford, D. J., Gasser, T., Ghattas, J., Gkritzalis, T., Grassi, G., Gregor, L., Gruber, N., Gürses, Ö., Harris, I., Hefner, M., Heinke, J., Houghton, R. A., Hurtt, G. C., Iida, Y., Ilyina, T., Jacobson, A. R., Jain, A., Jarníková, T., Jersild, A., Jiang, F., Jin, Z., Joos, F., Kato, E., Keeling, R. F., Kennedy, D., Klein Goldewijk, K., Knauer, J., Korsbakken, J. I., Körtzinger, A., Lan, X., Lefèvre, N., Li, H., Liu, J., Liu, Z., Ma, L., Marland, G., Mayot, N., McGuire, P. C., McKinley, G. A., Meyer, G., Morgan, E. J., Munro, D. R., Nakaoka, S.-I., Niwa, Y., O'Brien, K. M., Olsen, A., Omar, A. M., Ono, T., Paulsen, M., Pierrot, D., Pocock, K., Poulter, B., Powis, C. M., Rehder, G., Resplandy, L., Robertson, E., Rödenbeck, C., Rosan, T. M., Schwinger, J., Séférian, R., Smallman, T. L., Smith, S. M., Sospedra-Alfonso, R., Sun, Q., Sutton, A. J., Sweeney, C., Takao, S., Tans, P. P., Tian, H., Tilbrook, B., Tsujino, H., Tubiello, F., van der Werf, G. R., van Ooijen, E., Wanninkhof, R., Watanabe, M., Wimart-Rousseau, C., Yang, D., Yang, X., Yuan, W., Yue, X., Zaehle, S., Zeng, J., and Zheng, B.: Global Carbon Budget 2023, Earth Syst. Sci. Data, 15, 5301–5369, https://doi.org/10.5194/essd-15-5301-2023, 2023.

Goll, D. S., Joetzjer, E., Huang, M., and Ciais, P.: Low Phosphorus Availability Decreases Susceptibility of Tropical Primary Productivity to Droughts, Geophys. Res. Lett., 45, 8231–8240, https://doi.org/10.1029/2018GL077736, 2018.

Haverd, V., Smith, B., Nieradzik, L., Briggs, P. R., Woodgate, W., Trudinger, C. M., Canadell, J. G., and Cuntz, M.: A new version of the CABLE land surface model (Subversion revision r4601) incorporating land use and land cover change, woody vegetation

demography, and a novel optimisation-based approach to plant coordination of photosynthesis, Geosci. Model Dev., 11, 2995–3026, https://doi.org/10.5194/gmd-11-2995-2018, 2018.

He, W., Jiang, F., Ju, W., Byrne, B., Xiao, J., Nguyen, N. T., Wu, M., Wang, S., Wang, J., Rödenbeck, C., Li, X., Scholze, M., Monteil, G., Wang, H., Zhou, Y., He, Q., and Chen, J. M.: Do State-Of-The-Art Atmospheric CO_2 Inverse Models Capture Drought Impacts on the European Land Carbon Uptake?, J. Adv. Model. Earth Sy., 15, e2022MS003150, https://doi.org/10.1029/2022MS003150, 2023.

Jacobson, A. R., Schuldt, K. N., Tans, P., Arlyn Andrews, Miller, J. B., Oda, T., Mund, J., Weir, B., Ott, L., Aalto, T., Abshire, J. B., Aikin, K., Aoki, S., Apadula, F., Arnold, S., Baier, B., Bartyzel, J., Beyersdorf, A., Biermann, T., Biraud, S. C., Boenisch, H., Brailsford, G., Brand, W. A., Chen, G., Huilin Chen, Lukasz Chmura, Clark, S., Colomb, A., Commane, R., Conil, S., Couret, C., Cox, A., Cristofanelli, P., Cuevas, E., Curcoll, R., Daube, B., Davis, K. J., Wekker, S. de, Della Coletta, J., Delmotte, M., DiGangi, E., DiGangi, J. P., Di Sarra, A. G., Dlugokencky, E., Elkins, J. W., Emmenegger, L., Shuangxi Fang, Fischer, M. L., Forster, G., Frumau, A., Galkowski, M., Gatti, L. V., Gehrlein, T., Gerbig, C., Francois Gheusi, Gloor, E., Gomez-Trueba, V., Goto, D., Griffis, T., Hammer, S., Hanson, C., Haszpra, L., Hatakka, J., Heimann, M., Heliasz, M., Hensen, A., Hermansen, O., Hintsa, E., Holst, J., Ivakhov, V., Jaffe, D. A., Jordan, A., Joubert, W., Karion, A., Kawa, S. R., Kazan, V., Keeling, R. F., Keronen, P., Kneuer, T., Kolari, P., Kateřina Komínková, Kort, E., Kozlova, E., Krummel, P., Kubistin, D., Labuschagne, C., Lam, D. H., Lan, X., Langenfelds, R. L., Laurent, O., Laurila, T., Lauvaux, T., Lavric, J., Law, B. E., Lee, J., Lee, O. S., Lehner, I., Lehtinen, K., Leppert, R., Leskinen, A., Leuenberger, M., Levin, I., Levula, J., Lin, J., Lindauer, M., Loh, Z., Lopez, M., Luijkx, I. T., Lunder, C. R., Machida, T., Mammarella, I., Manca, G., Manning, A., Manning, A., Marek, M. V., Martin, M. Y., Matsueda, H., McKain, K., Meijer, H., Meinhardt, F., Merchant, L., N. Mihalopoulos, Miles, N. L., Miller, C. E., Mitchell, L., Mölder, M., Montzka, S., Moore, F., Moossen, H., Morgan, E., Josep-Anton Morgui, Morimoto, S., Müller-Williams, J., J. William Munger, Munro, D., Myhre, C. L., Shin-Ichiro Nakaoka, Jaroslaw Necki, Newman, S., Nichol, S., Niwa, Y., Obersteiner, F., O'Doherty, S., Paplawsky, B., Peischl, J., Peltola, O., Piacentino, S., Jean-Marc Pichon, Pickers, P., Piper, S., Pitt, J., Plass-Dülmer, C., Platt, S. M., Prinzivalli, S., Ramonet, M., Ramos, R., Reyes-Sanchez, E., Richardson, S. J., Riris, H., Rivas, P. P., Ryerson, T., Saito, K., Sargent, M., Sasakawa, M., Scheeren, B., Schuck, T., Schumacher, M., Seifert, T., Sha, M. K., Shepson, P., Shook, M., Sloop, C. D., Smith, P., Stanley, K., Steinbacher, M., Stephens, B., Sweeney, C., Thoning, K., Timas, H., Torn, M., Tørseth, K., Trisolino, P., Turnbull, J., van den Bulk, P., van Dinther, D., Vermeulen, A., Viner, B., Vitkova, G., Walker, S., Watson, A., Wofsy, S. C., Worsey, J., Worthy, D., Dickon Young, Zaehle, S., Zahn, A., and Zimnoch, M.: CarbonTracker CT2022, Global Monitoring Laboratory [data set], https://doi.org/10.25925/z1gj-3254, 2023 (data available at: https://gml.noaa.gov/aftp/products/carbontracker/co2/CT2022/fluxes/monthly/, last access: 17 April 2023 and https://gml.noaa.gov/aftp/products/carbontracker/co2/CT2022/molefractions/co2_total_monthly/, last access: 17 September 2024).

Jacobs, N., O'Dell, C. W., Taylor, T. E., Logan, T. L., Byrne, B., Kiel, M., Kivi, R., Heikkinen, P., Merrelli, A., Payne, V. H., and Chatterjee, A.: The importance of digital elevation model accuracy in X_{CO_2} retrievals: improving the Orbiting Carbon Observatory 2 Atmospheric Carbon Observations from Space version 11 retrieval product, Atmos. Meas. Tech., 17, 1375–1401, https://doi.org/10.5194/amt-17-1375-2024, 2024.

Jarvis, P., Rey, A., Petsikos, C., Wingate, L., Rayment, M., Pereira, J., Banza, J., David, J., Miglietta, F., Borghetti, M., Manca, G., and Valentini, R.: Drying and wetting of Mediterranean soils stimulates decomposition and carbon dioxide emission: the "Birch effect", Tree Physiol., 27, 929–940, https://doi.org/10.1093/treephys/27.7.929, 2007.

Joiner, J., Yoshida, Y., Zhang, Y., Duveiller, G., Jung, M., Lyapustin, A., Wang, Y., and Tucker, C. J.: Estimation of Terrestrial Global Gross Primary Production (GPP) with Satellite Data-Driven Models and Eddy Covariance Flux Data, Remote Sens., 10, 1346, https://doi.org/10.3390/rs10091346, 2018.

Joiner, J., Yoshida, Y., Koehler, P., Frankenberg, C., and Parazoo, N. C.: L2 Daily Solar-Induced Fluorescence (SIF) from MetOp-A GOME-2, 2007–2018, V2, ORNL DAAC, Oak Ridge, Tennessee, USA [data set], https://doi.org/10.3334/ORNLDAAC/2292, 2023 (data available at: https://search.earthdata.nasa.gov/, last access: 29 May 2024).

Jung, M., Schwalm, C., Migliavacca, M., Walther, S., Camps-Valls, G., Koirala, S., Anthoni, P., Besnard, S., Bodesheim, P., Carvalhais, N., Chevallier, F., Gans, F., Goll, D. S., Haverd, V., Köhler, P., Ichii, K., Jain, A. K., Liu, J., Lombardozzi, D., Nabel, J. E. M. S., Nelson, J. A., O'Sullivan, M., Pallandt, M., Papale, D., Peters, W., Pongratz, J., Rödenbeck, C., Sitch, S., Tramontana, G., Walker, A., Weber, U., and Reichstein, M.: Scaling carbon fluxes from eddy covariance sites to globe: synthesis and evaluation of the FLUXCOM approach, Biogeosciences, 17, 1343–1365, https://doi.org/10.5194/bg-17-1343-2020, 2020 (data available at: http://fluxcom.org/CF-Download/, last access: 21 January 2025).

Kaiser, J. W., Heil, A., Andreae, M. O., Benedetti, A., Chubarova, N., Jones, L., Morcrette, J.-J., Razinger, M., Schultz, M. G., Suttie, M., and van der Werf, G. R.: Biomass burning emissions estimated with a global fire assimilation system based on observed fire radiative power, Biogeosciences, 9, 527–554, https://doi.org/10.5194/bg-9-527-2012, 2012.

Kato, E., Kinoshita, T., Ito, A., Kawamiya, M., and Yamagata, Y.: Evaluation of spatially explicit emission scenario of land-use change and biomass burning using a process-based biogeochemical model, J. Land Use Sci., 8, 104–122, https://doi.org/10.1080/1747423X.2011.628705, 2013.

Krinner, G., Viovy, N., Noblet-Ducoudré, N. de, Ogée, J., Polcher, J., Friedlingstein, P., Ciais, P., Sitch, S., and Prentice, I. C.: A dynamic global vegetation model for studies of the coupled atmosphere-biosphere system, Global Biogeochem. Cy., 19, GB1015, https://doi.org/10.1029/2003GB002199, 2005.

Lasslop, G., Hantson, S., Harrison, S. P., Bachelet, D., Burton, C., Forkel, M., Forrest, M., Li, F., Melton, J. R., Yue, C., Archibald, S., Scheiter, S., Arneth, A., Hickler, T., and Sitch, S.: Global ecosystems and fire: Multi-model assessment of fire-induced tree-cover and carbon storage reduction, Glob. Change Biol., 26, 5027–5041, https://doi.org/10.1111/gcb.15160, 2020.

Lawrence, D. M., Fisher, R. A., Koven, C. D., Oleson, K. W., Swenson, S. C., Bonan, G., Collier, N., Ghimire, B., Kampenhout, L., Kennedy, D., Kluzek, E., Lawrence, P. J., Li, F., Li, H., Lombardozzi, D., Riley, W. J., Sacks, W. J., Shi, M., Vertenstein, M., Wieder, W. R., Xu, C., Ali, A. A., Badger, A. M., Bisht, G., Broeke, M., Brunke, M. A., Burns, S. P., Buzan, J., Clark, M., Craig, A., Dahlin, K., Drewniak, B., Fisher, J. B., Flanner, M., Fox, A. M., Gentine, P., Hoffman, F., Keppel-Aleks, G., Knox, R., Kumar, S., Lenaerts, J., Leung, L. R., Lipscomb, W. H., Lu, Y., Pandey, A., Pelletier, J. D., Perket, J., Randerson, J. T., Ricciuto, D. M., Sanderson, B. M., Slater, A., Subin, Z. M., Tang, J., Thomas, R. Q., Val Martin, M., and Zeng, X.: The Community Land Model Version 5: Description of New Features, Benchmarking, and Impact of Forcing Uncertainty, J. Adv. Model. Earth Sy., 11, 4245–4287, https://doi.org/10.1029/2018MS001583, 2019.

Le Quéré, C., Andres, R. J., Boden, T., Conway, T., Houghton, R. A., House, J. I., Marland, G., Peters, G. P., van der Werf, G. R., Ahlström, A., Andrew, R. M., Bopp, L., Canadell, J. G., Ciais, P., Doney, S. C., Enright, C., Friedlingstein, P., Huntingford, C., Jain, A. K., Jourdain, C., Kato, E., Keeling, R. F., Klein Goldewijk, K., Levis, S., Levy, P., Lomas, M., Poulter, B., Raupach, M. R., Schwinger, J., Sitch, S., Stocker, B. D., Viovy, N., Zaehle, S., and Zeng, N.: The global carbon budget 1959–2011, Earth Syst. Sci. Data, 5, 165–185, https://doi.org/10.5194/essd-5-165-2013, 2013.

Li, X., Xiao, J., He, B., Altaf Arain, M., Beringer, J., Desai, A. R., Emmel, C., Hollinger, D. Y., Krasnova, A., Mammarella, I., Noe, S. M., Ortiz, P. S., Rey-Sanchez, A. C., Rocha, A. V., and Varlagin, A.: Solar-induced chlorophyll fluorescence is strongly correlated with terrestrial photosynthesis for a wide variety of biomes: First global analysis based on OCO-2 and flux tower observations, Glob. Change Biol., 24, 3990–4008, https://doi.org/10.1111/gcb.14297, 2018.

Lienert, S. and Joos, F.: A Bayesian ensemble data assimilation to constrain model parameters and land-use carbon emissions, Biogeosciences, 15, 2909–2930, https://doi.org/10.5194/bg-15-2909-2018, 2018.

MacBean, N., Scott, R. L., Biederman, J. A., Peylin, P., Kolb, T., Litvak, M. E., Krishnan, P., Meyers, T. P., Arora, V. K., Bastrikov, V., Goll, D., Lombardozzi, D. L., Nabel, Julia E. M. S., Pongratz, J., Sitch, S., Walker, A. P., Zaehle, S., and Moore, D. J. P.: Dynamic global vegetation models underestimate net CO_2 flux mean and inter-annual variability in dryland ecosystems, Environ. Res. Lett., 16, 94023, https://doi.org/10.1088/1748-9326/ac1a38, 2021.

Masarie, K. A., Peters, W., Jacobson, A. R., and Tans, P. P.: ObsPack: a framework for the preparation, delivery, and attribution of atmospheric greenhouse gas measurements, Earth Syst. Sci. Data, 6, 375–384, https://doi.org/10.5194/essd-6-375-2014, 2014.

Meiyappan, P., Jain, A. K., and House, J. I.: Increased influence of nitrogen limitation on CO_2 emissions from future land use and land use change, Global Biogeochem. Cy., 29, 1524–1548, https://doi.org/10.1002/2015GB005086, 2015.

Melton, J. R., Arora, V. K., Wisernig-Cojoc, E., Seiler, C., Fortier, M., Chan, E., and Teckentrup, L.: CLASSIC v1.0: the open-source community successor to the Canadian Land Surface Scheme (CLASS) and the Canadian Terrestrial Ecosystem Model (CTEM) – Part 1: Model framework and site-level performance, Geosci. Model Dev., 13, 2825–2850, https://doi.org/10.5194/gmd-13-2825-2020, 2020.

Mengistu, A. G. and Mengistu Tsidu, G.: On the performance of satellite-based observations of XCO_2 in capturing the NOAA Carbon Tracker model and ground-based flask observations over Africa's land mass, Atmos. Meas. Tech., 13, 4009–4033, https://doi.org/10.5194/amt-13-4009-2020, 2020.

Metz, E.-M.: ATMO-IUP-UHEI/MetzEtAl2024: v1.0.0, Zenodo [code], https://doi.org/10.5281/zenodo.12528504, 2024.

Metz, E.-M., Vardag, S. N., Basu, S., Jung, M., Ahrens, B., El-Madany, T., Sitch, S., Arora, V. K., Briggs, P. R., Friedlingstein, P., Goll, D. S., Jain, A. K., Kato, E., Lombardozzi, D., Nabel, Julia E. M. S., Poulter, B., Séférian, R., Tian, H., Wiltshire, A., Yuan, W., Yue, X., Zaehle, S., Deutscher, N. M., Griffith, D. W. T., and Butz, A.: Soil respiration-driven CO_2 pulses dominate Australia's flux variability, Science, 379, 1332–1335, https://doi.org/10.1126/science.add7833, 2023.

Muñoz Sabater, J.: ERA5-Land monthly averaged data from 1950 to present, Copernicus Climate Change Service (C3S) Climate Data Store (CDS) [data set], https://doi.org/10.24381/cds.68d2bb30, 2019 (data available at: https://cds.climate.copernicus.eu/cdsapp#!/dataset/reanalysis-era5-land-monthly-means, last access: 13 October 2023).

NOAA: Global Monitoring Laboratory: Trends in Atmospheric Carbon Dioxide, https://www.esrl.noaa.gov/gmd/ccgg/trends/gl_gr.html, last access: 8 January 2024.

OCO-2/OCO-3 Science Team, Payne, V., and Chatterjee, A.: OCO-2 Level 2 bias-corrected XCO_2 and other select fields from the full-physics retrieval aggregated as daily files, Retrospective processing V11.1r, last access: 28 July 2020, Greenbelt, MD, USA, Goddard Earth Sciences Data and Information Services Center (GES DISC) [data set], https://doi.org/10.5067/8E4VLCK16O6Q, 2022.

OCO-2 Science Team, Gunson, M., and Eldering, A.: ACOS GOSAT/TANSO-FTS Level 2 bias-corrected XCO_2 and other select fields from the full-physics retrieval aggregated as daily files V9r, Greenbelt, MD, USA, Goddard Earth Sciences Data and Information Services Center (GES DISC) [data set], https://doi.org/10.5067/VWSABTO7ZII4, 2019 (data available at: https://oco2.gesdisc.eosdis.nasa.gov/data/GOSAT_TANSO_Level2/ACOS_L2_Lite_FP.9r/, last access: 28 July 2020).

Pandey, S., Miller, J. B., Basu, S., Liu, J., Weir, B., Byrne, B., Chevallier, F., Bowman, K. W., Liu, Z., Deng, F., O'Dell, C. W., and Chatterjee, A.: Toward low-latency estimation of atmospheric CO_2 growth rates using satellite observations: Evaluating sampling errors of satellite and in situ observing approaches, AGU Adv., 5, e2023AV001145, https://doi.org/10.1029/2023AV001145, 2024.

Pan, S., Yang, J., Tian, H., Shi, H., Chang, J., Ciais, P., Francois, L., Frieler, K., Fu, B., Hickler, T., Ito, A., Nishina, K., Ostberg, S., Reyer, C. P., Schaphoff, S., Steinkamp, J., and Zhao, F.: Climate Extreme Versus Carbon Extreme: Responses of Terrestrial Carbon Fluxes to Temperature and Precipitation, J. Geophys. Res.-Biogeo., 125, e2019JG005252, https://doi.org/10.1029/2019JG005252, 2020.

Peters, W., Jacobson, A. R., Sweeney, C., Andrews, A. E., Conway, T. J., Masarie, K., Miller, J. B., Bruhwiler, L. M. P., Pétron, G., Hirsch, A. I., Worthy, D. E. J., van der Werf, G. R., Ran-

derson, J. T., Wennberg, P. O., Krol, M. C., and Tans, P. P.: An atmospheric perspective on North American carbon dioxide exchange: CarbonTracker, P. Natl. Acad. Sci. USA, 104, 18925–18930, https://doi.org/10.1073/pnas.0708986104, 2007.

Piao, S., Wang, X., Wang, K., Li, X., Bastos, A., Canadell, J. G., Ciais, P., Friedlingstein, P., and Sitch, S.: Interannual variation of terrestrial carbon cycle: Issues and perspectives, Glob. Change Biol., 26, 300–318, https://doi.org/10.1111/gcb.14884, 2020.

Pierrat, Z., Magney, T., Parazoo, N. C., Grossmann, K., Bowling, D. R., Seibt, U., Johnson, B., Helgason, W., Barr, A., Bortnik, J., Norton, A., Maguire, A., Frankenberg, C., and Stutz, J.: Diurnal and Seasonal Dynamics of Solar-Induced Chlorophyll Fluorescence, Vegetation Indices, and Gross Primary Productivity in the Boreal Forest, J. Geophys. Res.-Biogeo., 127, e2021JG006588, https://doi.org/10.1029/2021JG006588, 2022.

Poulter, B., Ciais, P., Hodson, E., Lischke, H., Maignan, F., Plummer, S., and Zimmermann, N. E.: Plant functional type mapping for earth system models, Geosci. Model Dev., 4, 993–1010, https://doi.org/10.5194/gmd-4-993-2011, 2011.

Poulter, B., Frank, D., Ciais, P., Myneni, R. B., Andela, N., Bi, J., Broquet, G., Canadell, J. G., Chevallier, F., Liu, Y. Y., Running, S. W., Sitch, S., and van der Werf, G. R.: Contribution of semi-arid ecosystems to interannual variability of the global carbon cycle, Nature, 509, 600–603, https://doi.org/10.1038/nature13376, 2014.

Ramo, R., Roteta, E., Bistinas, I., van Wees, D., Bastarrika, A., Chuvieco, E., and van der Werf, G. R.: African burned area and fire carbon emissions are strongly impacted by small fires undetected by coarse resolution satellite data, P. Natl. Acad. Sci. USA, 118, e2011160118, https://doi.org/10.1073/pnas.2011160118, 2021.

Randerson, J. T., Thompson, M. V., Malmstrom, C. M., Field, C. B., and Fung, I. Y.: Substrate limitations for heterotrophs: Implications for models that estimate the seasonal cycle of atmospheric CO_2, Global Biogeochem. Cy., 10, 585–602, https://doi.org/10.1029/96GB01981, 1996.

Reick, C. H., Gayler, V., Goll, D., Hagemann, S., Heidkamp, M., Nabel, Julia E. M. S., Raddatz, T., Roeckner, E., Schnur, R., and Wilkenskjeld, S.: JSBACH 3 – The land component of the MPI Earth System Model: documentation of version 3.2, Reports on Earth System Science, 240, https://doi.org/10.17617/2.3279802, 2021.

Scholes, B.: FLUXNET2015 ZA-Kru Skukuza (2000–2013) [data set], last access: https://doi.org/10.18140/FLX/1440188, 2013 (data available at: https://fluxnet.org/data/fluxnet2015-dataset/, last access: 21 November 2023).

Sellar, A. A., Jones, C. G., Mulcahy, J. P., Tang, Y., Yool, A., Wiltshire, A., O'Connor, F. M., Stringer, M., Hill, R., Palmieri, J., Woodward, S., de Mora, L., Kuhlbrodt, T., Rumbold, S. T., Kelley, D. I., Ellis, R., Johnson, C. E., Walton, J., Abraham, N. L., Andrews, M. B., Andrews, T., Archibald, A. T., Berthou, S., Burke, E., Blockley, E., Carslaw, K., Dalvi, M., Edwards, J., Folberth, G. A., Gedney, N., Griffiths, P. T., Harper, A. B., Hendry, M. A., Hewitt, A. J., Johnson, B., Jones, A., Jones, C. D., Keeble, J., Liddicoat, S., Morgenstern, O., Parker, R. J., Predoi, V., Robertson, E., Siahaan, A., Smith, R. S., Swaminathan, R., Woodhouse, M. T., Zeng, G., and Zerroukat, M.: UKESM1: Description and evaluation of the UK Earth System Model, J. Adv. Model. Earth Sy., 11, 4513–4558, 2019.

Sellers, P. J., Schimel, D. S., Moore, B., Liu, J., and Eldering, A.: Observing carbon cycle–climate feedbacks from space, P. Natl. Acad. Sci. USA, 115, 7860–7868, https://doi.org/10.1073/pnas.1716613115, 2018.

Shi, Y., Matsunaga, T., Saito, M., Yamaguchi, Y., and Chen, X.: Comparison of global inventories of CO_2 emissions from biomass burning during 2002–2011 derived from multiple satellite products, Environ. Pollut., 206, 479–487, https://doi.org/10.1016/j.envpol.2015.08.009, 2015.

Sitch, S., Arora, V. K., Briggs, P., Friedlingstein, P., Goll, D. S., Jain, A. K., Kato, E., Krinner, G., Lienert, S., Lombardozzi, D., Nabel, J. E. M. S., Poulter, B., Séférian, R., Tian, H., Vuichard, N., Walker, A. P., Wiltshire, A., Yuan, W., Yue, X., and Zaehle, S.: TRENDY: Trends in the land carbon cycle, Trendy v9 [data set], available upon request at https://mdosullivan.github.io/GCB/ (last access: 24 January 2025), 2020.

Steiner, A. L.: Role of the Terrestrial Biosphere in Atmospheric Chemistry and Climate, Accounts Chem. Res., 53, 1260–1268, https://doi.org/10.1021/acs.accounts.0c00116, 2020.

Sun, Y., Frankenberg, C., Jung, M., Joiner, J., Guanter, L., Köhler, P., and Magney, T.: Overview of Solar-Induced chlorophyll Fluorescence (SIF) from the Orbiting Carbon Observatory-2: Retrieval, cross-mission comparison, and global monitoring for GPP, Remote Sens. Environ., 209, 808–823, https://doi.org/10.1016/j.rse.2018.02.016, 2018.

Taylor, T. E., O'Dell, C. W., Crisp, D., Kuze, A., Lindqvist, H., Wennberg, P. O., Chatterjee, A., Gunson, M., Eldering, A., Fisher, B., Kiel, M., Nelson, R. R., Merrelli, A., Osterman, G., Chevallier, F., Palmer, P. I., Feng, L., Deutscher, N. M., Dubey, M. K., Feist, D. G., García, O. E., Griffith, D. W. T., Hase, F., Iraci, L. T., Kivi, R., Liu, C., De Mazière, M., Morino, I., Notholt, J., Oh, Y.-S., Ohyama, H., Pollard, D. F., Rettinger, M., Schneider, M., Roehl, C. M., Sha, M. K., Shiomi, K., Strong, K., Sussmann, R., Té, Y., Velazco, V. A., Vrekoussis, M., Warneke, T., and Wunch, D.: An 11-year record of XCO_2 estimates derived from GOSAT measurements using the NASA ACOS version 9 retrieval algorithm, Earth Syst. Sci. Data, 14, 325–360, https://doi.org/10.5194/essd-14-325-2022, 2022.

Taylor, T. E., O'Dell, C. W., Baker, D., Bruegge, C., Chang, A., Chapsky, L., Chatterjee, A., Cheng, C., Chevallier, F., Crisp, D., Dang, L., Drouin, B., Eldering, A., Feng, L., Fisher, B., Fu, D., Gunson, M., Haemmerle, V., Keller, G. R., Kiel, M., Kuai, L., Kurosu, T., Lambert, A., Laughner, J., Lee, R., Liu, J., Mandrake, L., Marchetti, Y., McGarragh, G., Merrelli, A., Nelson, R. R., Osterman, G., Oyafuso, F., Palmer, P. I., Payne, V. H., Rosenberg, R., Somkuti, P., Spiers, G., To, C., Weir, B., Wennberg, P. O., Yu, S., and Zong, J.: Evaluating the consistency between OCO-2 and OCO-3 XCO_2 estimates derived from the NASA ACOS version 10 retrieval algorithm, Atmos. Meas. Tech., 16, 3173–3209, https://doi.org/10.5194/amt-16-3173-2023, 2023.

Tian, H., Chen, G., Lu, C., Xu, X., Hayes, D. J., Ren, W., Pan, S., Huntzinger, D. N., and Wofsy, S. C.: North American terrestrial CO_2 uptake largely offset by CH_4 and N_2O emissions: toward a full accounting of the greenhouse gas budget, Climatic Change, 129, 413–426, https://doi.org/10.1007/s10584-014-1072-9, 2015.

Tramontana, G., Jung, M., Schwalm, C. R., Ichii, K., Camps-Valls, G., Ráduly, B., Reichstein, M., Arain, M. A., Cescatti, A., Kiely, G., Merbold, L., Serrano-Ortiz, P., Sickert, S., Wolf, S., and Papale, D.: Predicting carbon dioxide and energy fluxes across global FLUXNET sites with regression algorithms, Biogeosciences, 13, 4291–4313, https://doi.org/10.5194/bg-13-4291-2016, 2016 (data available at: http://fluxcom.org/CF-Download/, last access: 21 January 2025).

Valentini, R., Arneth, A., Bombelli, A., Castaldi, S., Cazzolla Gatti, R., Chevallier, F., Ciais, P., Grieco, E., Hartmann, J., Henry, M., Houghton, R. A., Jung, M., Kutsch, W. L., Malhi, Y., Mayorga, E., Merbold, L., Murray-Tortarolo, G., Papale, D., Peylin, P., Poulter, B., Raymond, P. A., Santini, M., Sitch, S., Vaglio Laurin, G., van der Werf, G. R., Williams, C. A., and Scholes, R. J.: A full greenhouse gases budget of Africa: synthesis, uncertainties, and vulnerabilities, Biogeosciences, 11, 381–407, https://doi.org/10.5194/bg-11-381-2014, 2014.

van der Velde, I. R., van der Werf, G. R., van Wees, D., Schutgens, N. A. J., Vernooij, R., Houweling, S., Tonucci, E., Chuvieco, E., Randerson, J. T., Frey, M. M., Borsdorff, T., and Aben, I.: Small Fires, Big Impact: Evaluating Fire Emission Estimates in Southern Africa Using New Satellite Imagery of Burned Area and Carbon Monoxide, Geophys. Res. Lett., 51, e2023GL106122, https://doi.org/10.1029/2023GL106122, 2024.

van der Werf, G. R., Randerson, J. T., Giglio, L., van Leeuwen, T. T., Chen, Y., Rogers, B. M., Mu, M., van Marle, M. J. E., Morton, D. C., Collatz, G. J., Yokelson, R. J., and Kasibhatla, P. S.: Global Fire Emissions Database, Version 4.1 (GFED4s) [data set], https://www.geo.vu.nl/~gwerf/GFED/GFED4/ (last access: 10 July 2020), 2015.

van der Werf, G. R., Randerson, J. T., Giglio, L., van Leeuwen, T. T., Chen, Y., Rogers, B. M., Mu, M., van Marle, M. J. E., Morton, D. C., Collatz, G. J., Yokelson, R. J., and Kasibhatla, P. S.: Global fire emissions estimates during 1997–2016, Earth Syst. Sci. Data, 9, 697–720, https://doi.org/10.5194/essd-9-697-2017, 2017.

van Marle, M. J. E., Kloster, S., Magi, B. I., Marlon, J. R., Daniau, A.-L., Field, R. D., Arneth, A., Forrest, M., Hantson, S., Kehrwald, N. M., Knorr, W., Lasslop, G., Li, F., Mangeon, S., Yue, C., Kaiser, J. W., and van der Werf, G. R.: Historic global biomass burning emissions for CMIP6 (BB4CMIP) based on merging satellite observations with proxies and fire models (1750–2015), Geosci. Model Dev., 10, 3329–3357, https://doi.org/10.5194/gmd-10-3329-2017, 2017.

Vuichard, N., Messina, P., Luyssaert, S., Guenet, B., Zaehle, S., Ghattas, J., Bastrikov, V., and Peylin, P.: Accounting for carbon and nitrogen interactions in the global terrestrial ecosystem model ORCHIDEE (trunk version, rev 4999): multi-scale evaluation of gross primary production, Geosci. Model Dev., 12, 4751–4779, https://doi.org/10.5194/gmd-12-4751-2019, 2019.

Walker, A. P., Quaife, T., van Bodegom, P. M., Kauwe, M. G. de, Keenan, T. F., Joiner, J., Lomas, M. R., MacBean, N., Xu, C., Yang, X., and Woodward, F. I.: The impact of alternative trait-scaling hypotheses for the maximum photosynthetic carboxylation rate (Vcmax) on global gross primary production, New Phytol., 215, 1370–1386, https://doi.org/10.1111/nph.14623, 2017.

Weber, U., Jung, M., Reichstein, M., Beer, C., Braakhekke, M. C., Lehsten, V., Ghent, D., Kaduk, J., Viovy, N., Ciais, P., Gobron, N., and Rödenbeck, C.: The interannual variability of Africa's ecosystem productivity: a multi-model analysis, Biogeosciences, 6, 285–295, https://doi.org/10.5194/bg-6-285-2009, 2009.

Weir, B., Ott, L. E., Collatz, G. J., Kawa, S. R., Poulter, B., Chatterjee, A., Oda, T., and Pawson, S.: Bias-correcting carbon fluxes derived from land-surface satellite data for retrospective and near-real-time assimilation systems, Atmos. Chem. Phys., 21, 9609–9628, https://doi.org/10.5194/acp-21-9609-2021, 2021.

Wiedinmyer, C., Akagi, S. K., Yokelson, R. J., Emmons, L. K., Al-Saadi, J. A., Orlando, J. J., and Soja, A. J.: The Fire INventory from NCAR (FINN): a high resolution global model to estimate the emissions from open burning, Geosci. Model Dev., 4, 625–641, https://doi.org/10.5194/gmd-4-625-2011, 2011.

Wiedinmyer, C., Akagi, S. K., Yokelson, R. J., Emmons, L. K., Al-Saadi, J. A., Orlando, J. J., and Soja, A. J.: Fire INventory from NCAR (FINN), Version 1.5 [data set], https://www.acom.ucar.edu/Data/fire/ (last access: 18 November 2020), 2021.

Williams, C. A., Hanan, N. P., Neff, J. C., Scholes, R. J., Berry, J. A., Denning, A. S., and Baker, D. F.: Africa and the global carbon cycle, Carbon balance and management, 2, 3, https://doi.org/10.1186/1750-0680-2-3, 2007.

Williams, C. A., Hanan, N. P., Baker, I., COLLATZ, G. J., Berry, J., and Denning, A. S.: Interannual variability of photosynthesis across Africa and its attribution, J. Geophys. Res., 113, G04015, https://doi.org/10.1029/2008JG000718, 2008.

Wunch, D., Toon, G. C., Blavier, J.-F. L., Washenfelder, R. A., Notholt, J., Connor, B. J., Griffith, D. W. T., Sherlock, V., and Wennberg, P. O.: The Total Carbon Column Observing Network, Philos. T. Roy. Soc. A., 369, 2087–2112, https://doi.org/10.1098/rsta.2010.0240, 2011.

Yuan, W., Liu, D., Dong, W., Liu, S., Zhou, G., Yu, G., Zhao, T., Feng, J., Ma, Z., Chen, J., Chen, Y., Chen, S., Han, S., Huang, J., Li, L., Liu, H., Liu, S., Ma, M., Wang, Y., Xia, J., Xu, W., Zhang, Q., Zhao, X., and Zhao, L.: Multi-year precipitation reduction strongly decreases carbon uptake over northern China, J. Geophys. Res.-Biogeo., 119, 881–896, https://doi.org/10.1002/2014JG002608, 2014.

Yue, X. and Unger, N.: The Yale Interactive terrestrial Biosphere model version 1.0: description, evaluation and implementation into NASA GISS ModelE2, Geosci. Model Dev., 8, 2399–2417, https://doi.org/10.5194/gmd-8-2399-2015, 2015.

Zaehle, S., Friend, A. D., Friedlingstein, P., Dentener, F., Peylin, P., and Schulz, M.: Carbon and nitrogen cycle dynamics in the O-CN land surface model: 2. Role of the nitrogen cycle in the historical terrestrial carbon balance, Global Biogeochem. Cy., 24, GB1006, https://doi.org/10.1029/2009GB003522, 2010.

Zeng, N., Mariotti, A., and Wetzel, P.: Terrestrial mechanisms of interannual CO_2 variability, Global Biogeochem. Cy., 19, GB1016, https://doi.org/10.1029/2004gb002273, 2005.

Zhang, X., Wang, Y.-P., Peng, S., Rayner, P. J., Ciais, P., Silver, J. D., Piao, S., Zhu, Z., Lu, X., and Zheng, X.: Dominant regions and drivers of the variability of the global land carbon sink across timescales, Glob. Change Biol., 24, 3954–3968, https://doi.org/10.1111/gcb.14275, 2018.

Zhang, Y., Guanter, L., Berry, J. A., van der Tol, C., Yang, X., Tang, J., and Zhang, F.: Model-based analysis of the relationship between sun-induced chlorophyll fluorescence and gross primary production for remote sensing applications, Remote Sens. Environ., 187, 145–155, https://doi.org/10.1016/j.rse.2016.10.016, 2016a.

Zhang, Y., Xiao, X., Jin, C., Dong, J., Zhou, S., Wagle, P., Joiner, J., Guanter, L., Zhang, Y., Zhang, G., Qin, Y., Wang, J., and Moore, B.: Consistency between sun-induced chlorophyll fluorescence and gross primary production of vegetation in North America, Remote Sens. Environ., 183, 154–169, https://doi.org/10.1016/j.rse.2016.05.015, 2016b.